

Impact of sea-ice model complexity on the performance of an unstructured-mesh sea-ice/ocean model under different atmospheric forcings

Lorenzo Zampieri¹, Frank Kauker¹, Jörg Fröhle², Hiroshi Sumata³, Elizabeth C Hunke⁴, and Helge Goessling¹

¹Alfred Wegener Institute Helmholtz Centre for Polar and Marine Research

²Kiel University

³Norwegian Polar Institute, Fram Centre

⁴Los Alamos National Laboratory

November 21, 2022

Abstract

We have equipped the unstructured-mesh global sea-ice and ocean model FESOM2 with a set of physical parameterizations derived from the single-column sea-ice model Icepack. The update has substantially broadened the range of physical processes that can be represented by the model. The new features are directly implemented on the unstructured FESOM2 mesh, and thereby benefit from the flexibility that comes with it in terms of spatial resolution. A subset of the parameter space of three model configurations, with increasing complexity, has been calibrated with an iterative Green's function optimization method to test fairly the impact of the model update on the sea-ice representation. Furthermore, to explore the sensitivity of the results to different atmospheric forcings, each model configuration was calibrated separately for the NCEP-CFSR/CFSv2 and ERA5 forcings. The results suggest that a complex model formulation leads to a better agreement between modeled and the observed sea-ice concentration and snow thickness, while differences are smaller for sea-ice thickness and drift speed. However, the choice of the atmospheric forcing also impacts the agreement of FESOM2 simulations and observations, with NCEP-CFSR/CFSv2 being particularly beneficial for the simulated sea-ice concentration and ERA5 for sea-ice drift speed. In this respect, our results indicate that the parameter calibration can better compensate for differences among atmospheric forcings in a simpler model (i.e. sea-ice has no heat capacity) than in more energy consistent formulations with a prognostic ice thickness distribution.

Impact of sea-ice model complexity on the performance of an unstructured-mesh sea-ice/ocean model under different atmospheric forcings

L. Zampieri^{1*}, F. Kauker^{1,2}, J. Fröhle³, H. Sumata⁴, E. C. Hunke⁵,
H. F. Goessling¹

¹Alfred Wegener Institute, Helmholtz Centre for Polar and Marine Research, Bremerhaven, Germany

²Atmosphere Ocean Systems, Hamburg, Germany

³Kiel University, Kiel, Germany

⁴Norwegian Polar Institute, Fram Centre, Tromsø, Norway

⁵Los Alamos National Laboratory, Los Alamos, NM, USA

Key Points:

- Increased sea-ice model complexity improves the simulated sea-ice concentration and snow thickness.
- Sea-ice thickness and drift are only weakly affected by model complexity.
- Parameter calibration can better compensate for differences between atmospheric forcings in a simpler model.

Corresponding author: Lorenzo Zampieri, lorenzo.zampieri@awi.de

Abstract

We have equipped the unstructured-mesh global sea-ice and ocean model FESOM2 with a set of physical parameterizations derived from the single-column sea-ice model Icepack. The update has substantially broadened the range of physical processes that can be represented by the model. The new features are directly implemented on the unstructured FESOM2 mesh, and thereby benefit from the flexibility that comes with it in terms of spatial resolution. A subset of the parameter space of three model configurations, with increasing complexity, has been calibrated with an iterative Green's function optimization method to test fairly the impact of the model update on the sea-ice representation. Furthermore, to explore the sensitivity of the results to different atmospheric forcings, each model configuration was calibrated separately for the NCEP-CFSR/CFSv2 and ERA5 forcings. The results suggest that a complex model formulation leads to a better agreement between modeled and the observed sea-ice concentration and snow thickness, while differences are smaller for sea-ice thickness and drift speed. However, the choice of the atmospheric forcing also impacts the agreement of the FESOM2 simulations and observations, with NCEP-CFSR/CFSv2 being particularly beneficial for the simulated sea-ice concentration and ERA5 for sea-ice drift speed. In this respect, our results indicate that the parameter calibration can better compensate for differences among atmospheric forcings in a simpler model (i.e. sea-ice has no heat capacity) than in more energy consistent formulations with a prognostic ice thickness distribution.

Plain Language Summary

The role of model complexity in determining the performance of sea-ice numerical simulations is still not completely understood. Some studies suggest that a more sophisticated description of the sea-ice physics leads to simulations that agree better with sea-ice observations. Others, however, fail to establish a link between complex model formulations and improved model performance. Here, we investigate this open question by analyzing a set of sea-ice simulations performed with a revised and improved sea-ice model that features substantial modularity in terms of model complexity. Ten model parameters of three different model configurations are optimized to improve the agreement between model results and observations, allowing a fair comparison between model configurations with varying complexity. The model optimization is repeated for two different atmospheric forcings to shed light on the relationship between model complexity and other sources of uncertainty in the sea-ice simulations, such as those associated with the atmospheric conditions. The results suggest that an elaborated formulation of our model can lead to a more appropriate representation of sea ice concentration and snow thickness, while it is less relevant for sea-ice thickness and drift.

1 Introduction

Sea-ice is a key component of the climate system (Dieckmann & Hellmer, 2010) and it plays a central role as a physical regulator of the energy exchange between atmosphere and ocean in polar regions (Döscher et al., 2014). Furthermore, sea-ice represents by itself a platform where large ecosystems thrive (Spindler, 1994), and it is a fundamental element in the lives of coastal human communities in the Arctic (Cooley et al., 2020). Because of the strong and rapid transformations that sea-ice has undergone in recent years due to global warming (particularly in the Arctic; Notz & Stroeve (2016)), there is an urgent need to better understand and being able to quantify the physical and biogeochemical mechanisms regulating the sea-ice system, to inform decision-makers and various stakeholders. Reliable dynamical sea-ice models can be fundamental tools for accurately predicting the evolution of sea ice at multiple timescales, from days to centuries into the future.

In the past decades, there has been a constant development of more complex and physically consistent sea-ice model formulations, summarized by Hunke et al. (2010) and Notz (2012), and of which we give a brief overview in Sec. 2.2. At the same time, the resolution of sea-ice and ocean models has increased due to the growing availability of computational resources, and so has the resolution and quality of the atmospheric reanalyses used to force the models. These developments, together with the growing availability of more accurate sea-ice observations to constrain our models, have led to better sea-ice simulations. Multiple studies attribute a relevant role in improving the sea-ice model performance to more realistic model formulations (Vancoppenolle et al. (2009); Massonnet et al. (2011); Flocco et al. (2012); Roach, Horvat, et al. (2018), among others). However, in the framework of the Coupled Model Intercomparison Project (CMIP), the SIMIP Community (2020) (Sea Ice Model Intercomparison Project) shows that it is unclear to what degree differences between CMIP6, CMIP5, and CMIP3 sea-ice simulations are caused by better model physics versus other changes in the forcing. In the field of subseasonal and seasonal sea-ice forecasting, simple dynamical models exhibit predictive skills comparable to or even better than those of more complex forecast systems (Zampieri et al., 2018, 2019), suggesting that the year-to-year variability, the skill of the atmospheric models, and the quality of initial conditions dominate the variation in ensemble prediction success (Stroeve et al., 2014). In conclusion, to what extent the model complexity impacts the quality of sea-ice simulations remains an open question always evolving with our models (Blockley et al., 2020).

A key aspect to examine when assessing the relative performance of multiple model formulations is whether these are all appropriately tuned (Miller et al., 2006). Because of an interdependency of model parameters and a lack of comprehensive ice and snow observations, the model parameters are in general underconstrained (Urrego-Blanco et al., 2016), and their systematic calibration can substantially impact the quality of the simulations (J. Turner et al., 2013; Massonnet et al., 2014; Ungermann et al., 2017; Sumata et al., 2019a; Roach, Tett, et al., 2018). Furthermore, acknowledging the substantial differences between the reanalysis products used to force the sea-ice models in stand-alone setups (Batrak & Müller, 2019), we argue that the same model configuration should be also optimized separately for different forcing conditions. As shown by Bitz et al. (2002) and Miller et al. (2007), the behavior of a specific model formulation can change substantially based on the forcing used.

Most of the relevant sea-ice parameterizations and modeling strategies developed over the years have been collected by the scientific community and integrated into sophisticated sea-ice models, the most advanced and complete of which is arguably CICE (Hunke et al., 2020a). The CICE model is distributed in combination with the Icepack column-physics package (Hunke et al., 2020b) – a collection of physical parameterizations that account for thermodynamic and mechanic sub-grid processes not explicitly resolved by the models. Because of its modularity, Icepack can be conveniently implemented in ocean and sea-ice models other than CICE. In this regard, this study presents a new version of the Finite-volume Sea ice-Ocean Model version 2 (FESOM2; Danilov et al. (2017)) that exploits the capabilities of the Icepack column physics package. As we describe in Sec. 2.2, the development of the FESOM2 sea-ice component has been mostly focused on dynamical aspects, while the adopted sub-grid sea-ice parameterizations were quite simple and outdated if compared to those implemented in other sea-ice models. This resulted in a partially inconsistent physical formulation of the standard FESOM2 model, caused for example by the missing representation of the sea-ice internal energy. The inclusion of Icepack in FESOM2 has substantially broadened the range of sea-ice physical processes that can be simulated by the FESOM2 model, making it an ideal tool for answering the scientific questions posed below.

Based on the new FESOM2-Icepack implementation, we designed a set of experiments to assess the impact of the sea-ice model complexity on the quality of the sea-ice simulations. Ten parameters from three distinct model setups are optimized with a semi-automated calibration technique and compared to different types of sea-ice and snow observations. Be-

cause we deal with a standalone ocean and sea-ice model (i.e. no coupling to an atmospheric model) the calibration process is conducted separately for two different atmospheric reanalysis products used to force FESOM2. Based on the outcome of the calibration and the resulting model performance, we try to address the following questions:

1. Does a more complex and physically consistent formulation of the sea-ice model lead to better sea-ice simulations given the resolution, coverage and uncertainty of satellite Earth Observations (EO) of the sea-ice available today?
2. How does the impact of different atmospheric forcings on the sea-ice model performance relate to the impact of model complexity?
3. Which sea-ice formulation can be calibrated more effectively?

The remainder of this paper is organized as follows: the method section presents the standard (Sec. 2.1) and Icepack (Sec. 2.2) FESOM2 formulations, followed by the theoretical description of the Green’s function approach for the calibration of the model parameter space (Sec. 2.3). We then describe the experimental setups employed in the study and we present the practical implementation of the calibration technique (Sec. 2.4), as well as the observations used for constraining the parameter space and for validating the model results (Sec. 2.5). The results section (Sec. 3) describes the impact of the parameter optimization on the model performance in terms of cost function reduction. Furthermore, we explore the discrepancies of the various optimized model configurations by comparing the simulated sea-ice and snow state to different types of observations, and by linking this to differences in the optimized model parameters. Finally, the computational performance of three model setups is analyzed for assessing the sustainability of more sophisticated, and thus computationally more demanding, sea-ice setups for diverse modeling applications (Sec. 4.3).

2 Methods

2.1 Standard sea-ice formulation in FESOM2

Danilov et al. (2015) describes in detail the numerical implementation of the Finite Element Sea-Ice Model (FESIM), which is the standard sea-ice component of FESOM2. Three alternative algorithms are available for solving the sea-ice momentum equation: a classical elastic-viscous-plastic (EVP) approach coded following Hunke & Dukowicz (1997) plus two modified versions of the EVP solver: the modified EVP (mEVP; Kimmritz et al.

(2015)), and the adaptive EVP (aEVP; Kimmritz et al. (2016)). Three sea-ice tracers are advected based on a finite element (FE) flux corrected transport (FCT) scheme (Löhner et al., 1987): the sea-ice area fraction a_i , and the sea-ice and snow volumes per unit area, v_i and v_s . The thermodynamic evolution of sea ice is described by a simple 0-layer model (i.e. the sea-ice and snow layers have no heat capacity) that follows Parkinson & Washington (1979). The interaction between the radiation and sea ice is mediated by four constant albedo values (dry ice, wet (melting) ice, dry snow, and wet (melting) snow) that respond to changes in the atmospheric near-surface temperature, thus including an implicit description of the radiative effect of melt ponds during the melting season. No incoming shortwave radiation penetrates through the snow and sea-ice layers.

2.2 Icepack implementation in FESOM2

Icepack (Hunke et al., 2020b) – the column physics package of the sea-ice model CICE – is a collection of physical parameterizations that account for thermodynamic and mechanic sub-grid processes not explicitly resolved by the hosting sea-ice model. The modular implementation of Icepack allows the users to vary substantially the complexity of the sea-ice model, with the possibility of choosing between several schemes and a broad set of active and passive tracers that describe the sea-ice state. Similarly to FESIM, Icepack can make use of a simple 0-layer sea-ice and snow thermodynamics scheme (Semtner, 1976). However, two more sophisticated and energy consistent multi-layer thermodynamics formulations, taking into account the sea-ice enthalpy and salinity, are also available: the Bitz & Lipscomb (1999) thermodynamics (BL99 hereafter), which assumes a temporally constant sea-ice salinity profile, and the “mushy layer” implementation, with a prognostic sea-ice salinity description (A. K. Turner et al., 2013). To account for the sea-ice thickness variations typically observed at sub-grid scales, Icepack discretizes the sea-ice cover in multiple classes, each representative of a sea-ice thickness range, and describes prognostically the evolution of the Ice Thickness Distribution (ITD) in time and space (Bitz et al., 2001). The processes leading to changes in the ITD are sea-ice growth and melt, snow-ice formation (flooding), and mechanical redistribution (i.e. sea-ice ridging and rafting due to dynamical deformation; Lipscomb et al. (2007)). In terms of the interaction between sea ice and radiation, Icepack includes two more sophisticated parameterizations in addition to a simple albedo scheme similar to that of FESIM. In the “CCSM3” formulation, the surface albedo depends on the sea-ice and snow thickness and temperature, and it is defined separately for

the visible and infrared portion of the spectrum. The main difference between this and the constant albedo approach is a reduction of the surface reflectivity for thin sea-ice or snow. The even more sophisticated “Delta-Eddington” formulation exploits the inherent optical properties of snow and sea ice for solving the radiation budget (Holland et al., 2012), and it can be combined with three explicit prognostic melt pond schemes (Holland et al., 2012; Flocco et al., 2010; Hunke et al., 2013). Finally, the Icepack radiation implementation allows the penetration of part of the incoming shortwave radiation through snow and sea ice, leading to additional energy absorption in the water column below the sea ice.

Icepack v1.2.1 has been implemented in FESOM2 and can now be used as an alternative to the standard FESIM thermodynamic module. As the standard FESIM implementation, the Icepack column-physics subroutines run every ocean time step. All the Icepack variables are defined directly on the FESOM2 mesh, ensuring an optimal consistency between the ocean and the sea-ice components of the model. The inclusion of Icepack in FESOM2 required a revision of the calling sequence within the sea-ice model (Fig. 1), which now follows that of the CICE model (Hunke et al., 2020a). The coefficients mediating the momentum and heat exchanges between atmosphere and ice, previously constant in FESIM, have been updated and are now computed iteratively based on the stability of the atmospheric near-surface layer (Jordan et al., 1999). The solution of the momentum equation for computing the sea-ice velocity does not change when running in FESOM2-Icepack configuration. Two alternative formulations of the sea-ice strength P are available in Icepack and can be used in the EVP solver:

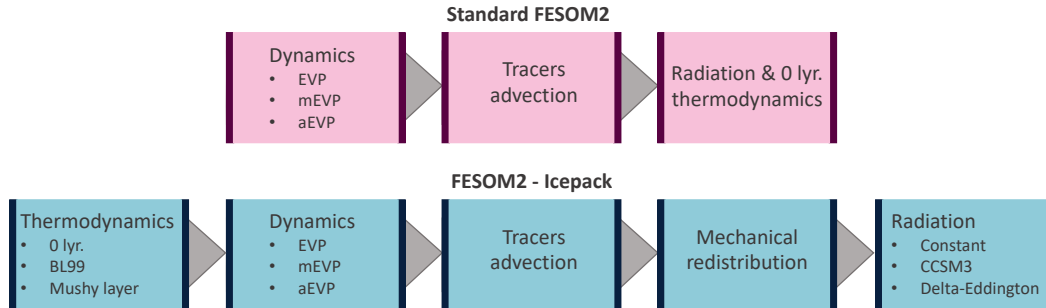


Figure 1. Schematic describing the calling sequences of the Standard FESOM2 and FESOM2-Icepack implementations.

$$\text{Hibler (1979): } P = P^* v e^{-C^*(1-a_i)} \quad (1)$$

$$\text{Rothrock (1975): } P = C_p C_f \int_0^\infty h^2 \omega_r(h) dh \quad (2)$$

where $h = v/a$ is the ice thickness, P^* , C^* , and C_f are empirical parameters, $C_p = \rho_i(\rho_w - \rho_i)g/(2\rho_w)$ is a combination of the gravitational acceleration and the densities of ice and water, and $\omega_r(h)$ is a function that represents the effective sea-ice volume change for each thickness class due to mechanical redistribution processes. In this study, the Hibler (1979) approach (H79 hereafter) is adopted for all model setups instead of the Rothrock (1975) approach (R75 hereafter). The reasoning behind this choice will be discussed in Sec. 2.4.

In the FESOM2 implementation of Icepack, each tracer is advected separately using the FE-FCT scheme by Löhner et al. (1987) as described in Kuzmin (2009). The tracer advection is based on the conservation equation

$$\partial_t T + \nabla \cdot (T \mathbf{v}) = 0, \quad (3)$$

where T is a generic advected tracer with no dependencies and \mathbf{v} is the sea-ice velocity that solves the momentum equation. If a tracer T_2 depends on another tracer T_1 , the advected quantity that satisfies Eq. 3 is $T = T_1 T_2$. This concept can be generalized for a tracer with more than one dependency. Icepack comes with a vast set of required and optional tracers. As for the standard FESIM, a_i , v_i , and v_s are required tracers. However, in Icepack these three variables are defined separately for each ice thickness class. The skin temperature of the sea-ice, or in the presence of snow of the snow, T_s is also defined separately for each thickness class and depends on a_i for the advection. If the BL99 or mushy thermodynamics are used, the enthalpy of sea-ice and snow layers (q_i, q_s), and the sea-ice salinity s_i become also required tracers and depend on v_i or v_s . Several more tracers are available (melt pond fraction and depth, sea-ice age, first-year ice fraction, level ice fraction and volume, etc.) depending on the chosen setup of the model. All these tracers are implemented in the FESOM2-Icepack model.

2.3 Green's function approach for the optimization of the model parameters

The Green's function approach is a simple, yet powerful method that, given some observations, can be used for the calibration of the parameter space of general circulation models (Stammer & Wunsch, 1996; Menemenlis & Wunsch, 1997; Menemenlis et al., 2005;

Nguyen et al., 2011; Ungermann et al., 2017). The practical realization of one iteration of this method requires to compute an ensemble of n sensitivity simulations by perturbing separately each one of the n parameters that we choose to optimize. The Green's functions of these sensitivity simulations are then combined through discrete inverse theory for constructing an optimal linear solution that minimizes the difference between the model state and the observations, and which corresponds to a set of optimal parameter perturbations. Menemenlis et al. (2005) and Ungermann et al. (2017) provide an extensive mathematical derivation of the method. Here, we limit our description to a few important points.

Given a vector of m observations \mathbf{y} and their measurement uncertainties σ , the relationship between the observations and a model operator G can be expressed as

$$\mathbf{y} = G(\boldsymbol{\nu}) + \boldsymbol{\epsilon} , \quad (4)$$

where $\boldsymbol{\nu}$ contains a generic set of n parameter perturbations around a reference state $\boldsymbol{\nu}_0$, and $\boldsymbol{\epsilon}$ represents the discrepancy between the observations and the model results. The optimal set of parameters $\boldsymbol{\nu}_{opt}$ can be obtained by minimizing a quadratic cost function

$$F = \boldsymbol{\epsilon}^T \mathbf{R} \boldsymbol{\epsilon} , \quad (5)$$

where \mathbf{R} , the covariance matrix of $\boldsymbol{\epsilon}$, is assumed to be a simple diagonal matrix with elements $R_{ij} = (\sigma_i)^{-2}$ (with $i, j = 1 \dots m$), meaning that observation errors are considered independent. In this study, each element of \mathbf{R} is further divided by the total number of observations of its corresponding observation type. In this way, the same weight is given to each observational type employed in the optimization. Let us assume for now that a linearization of the system holds (we will discuss this aspect further in Sec. 4.2), and that the model operator G can be represented by a matrix \mathbf{G} , so that the misfit between observations and the control simulation (for which $\boldsymbol{\nu} = 0$) can be expressed as

$$\Delta \mathbf{y} = \mathbf{y} - G(0) = \mathbf{G} \boldsymbol{\nu} + \boldsymbol{\epsilon} . \quad (6)$$

In practice, \mathbf{G} is an $m \times n$ matrix constructed by combining the Green's function for each of the parameter perturbations $\boldsymbol{\nu} = (\nu_1 \dots \nu_n)$. Specifically, \mathbf{g}_j —the j^{th} -column of the matrix \mathbf{G} —is

$$\mathbf{g}_j = \frac{G(\boldsymbol{\nu}_j) - G(0)}{\nu_j}, \quad (7)$$

where $G(\boldsymbol{\nu}_j)$ is the sensitivity simulation where only the parameter ν_j is perturbed. The set of optimal parameters that minimizes the cost function is given by

$$\boldsymbol{\nu}_{opt} = \boldsymbol{\nu}_0 + (\mathbf{G}^T \mathbf{R} \mathbf{G})^{-1} \mathbf{G}^T \mathbf{R} \Delta \mathbf{y}. \quad (8)$$

2.4 Model simulations

All model simulations are run on a global mesh with 1.27×10^5 surface nodes and 46 ocean vertical levels. This unstructured mesh has approximately a 1° resolution over most of the domain, but it is refined along the coastlines, in the equatorial regions, and north of 50°N , where the resolution reaches $\sim 25\text{km}$ (see Fig. 4a in Sein et al. (2016) for more details on the mesh). The atmospheric boundary conditions used to force the FESOM2 model are derived from two reanalysis products: the European Centre for Medium-Range Weather Forecasts Reanalysis 5th Generation (ERA5) global reanalysis (Hersbach et al., 2020) and the NCEP Climate Forecast System (NCEP hereafter; Saha et al. (2010, 2014)). The fields used to force the model are the 2-m air temperature and specific humidity, the 10-m wind velocity, the downward longwave and shortwave radiation, and both liquid and solid precipitation. The ocean component of the FESOM2 model is initialized in 1980 from the PHC3 ocean climatology (Steele et al., 2001). A sea-ice thickness of 2m is set at initial time in regions with sea surface temperature below -1.8°C .

The Green's function approach for parameter optimization is applied to three different model setups of increasing complexity:

- C1** Low-complexity configuration corresponding to the standard FESIM implementation within FESOM2, as described in Sec. 2.1.
- C2** Medium-complexity configuration based on the FESOM2-Icepack implementation described in Sec. 2.2. This configuration features an ITD with 5 thickness classes, the BL99 thermodynamics (4 sea-ice layers and 1 snow layer), and the CCSM3 radiation scheme.
- C3** High-complexity configuration based on the FESOM2-Icepack implementation. Like C2, C3 features an ITD with 5 thickness classes and the BL99 thermodynamics with

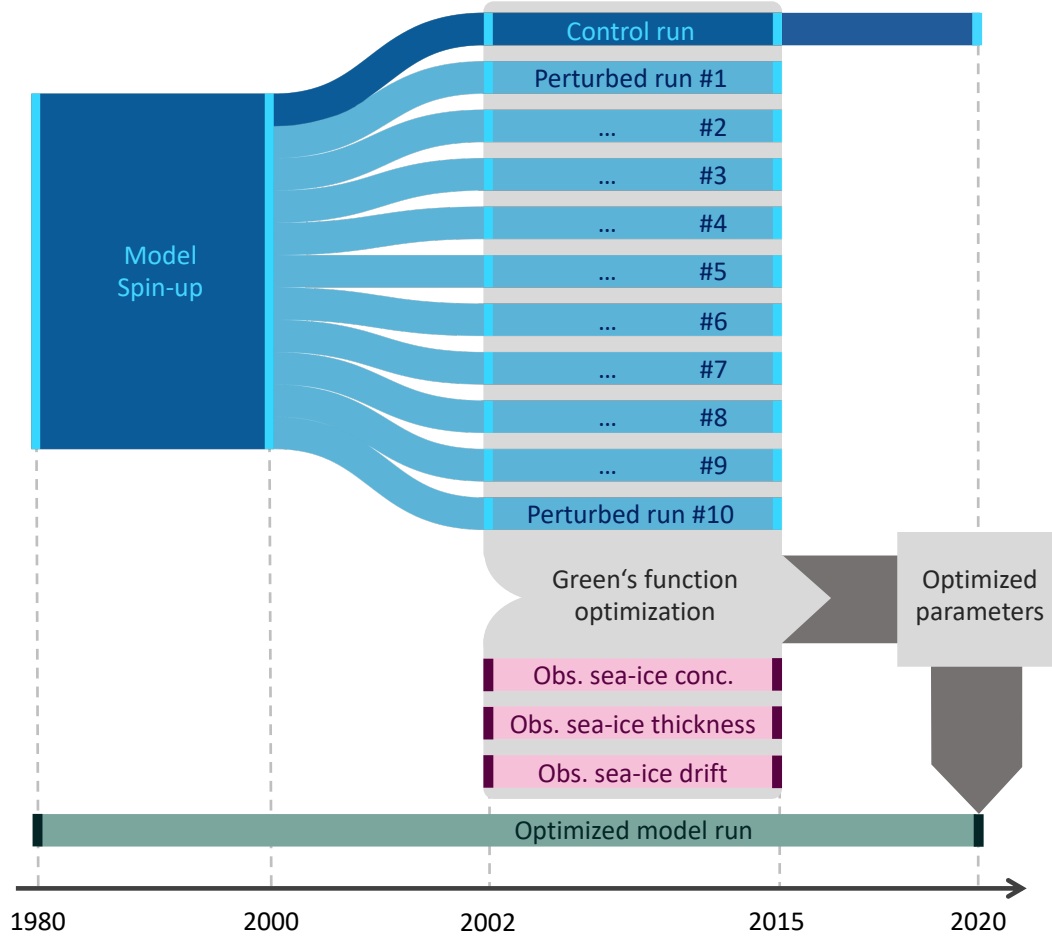


Figure 2. Schematic of one iteration of the Green’s function approach for parameter optimization as employed in our study for each configuration. When the second iteration is performed, the optimized model run computed at the end of the first iteration serves as control run for the second one.

269 4+1 vertical layers. The CCSM3 radiation is replaced by the Delta-Eddington scheme,
 270 and the melt ponds are prognostically described with the CESM parameterizations
 271 (Holland et al., 2012).

272 The Icespack configurations C2 and C3 resemble the sea-ice formulation of the climate
 273 models CCSM3 (Collins et al., 2006) and CCSM4/CESM1 (Jahn et al., 2012) respectively.
 274 The three configurations are optimized twice, once for each atmospheric forcing employed:
 275 ERA5 (suffix “E” hereafter) and NCEP (suffix “N” hereafter). This leads to a total of 6
 276 optimal parameter sets, each one optimized by performing two iterations of the Green’s
 277 function method. A schematic of the Green’s function optimization procedure is displayed

in Fig. 2. Each configuration undergoes a 20-year spin-up (1980–1999) to guarantee a realistic state of the modelled upper ocean (upper 1000 m) and of the sea-ice cover in (quasi-)equilibrium with the chosen atmospheric forcing product and the individual parameter set. The model optimization window is limited to the 14-year period 2002–2015, i.e. the cost function is evaluated in this period. 2000 and 2001 are additional spin-up years for ensuring a full response to each sea-ice parameter perturbation (Fig. 2).

The R75 formulation of the sea-ice strength is arguably more physically consistent than the H79 formulation, as it includes information about the ITD in each grid cell and it considers potential energy changes associated with the redistribution. However, Ungermann et al. (2017) show that the H79 approach leads to a better fit between model data and observations when properly tuned. In addition, the R75 sea-ice strength is much more non-linear than H79 one. For these reasons, and for being able to compare the C1 setup (no ITD; only H79 available) to the C2 and C3 setups (with ITD; both H79 and R75 available), all the simulations here presented employ the H79 sea-ice strength formulation.

Because the finite availability of computational resources limits in practice the number of parameters that can be optimized with the Green’s function approach (a separate sensitivity run is needed for each parameter one intends to optimize), the parameters have been chosen based on their ability to influence the sea-ice state of the model, as described in previous studies (Massonnet et al., 2014; Urrego-Blanco et al., 2016; Ungermann et al., 2017; Sumata et al., 2019a). In total, 10 model parameters are optimized for each of the three model setups (Tab. 1). The chosen parameters act on various sea-ice parameterizations: thermodynamics, dynamics, radiation, and mechanical redistribution. Some are common to all three configurations (α_O , k_S , P^* , C^* , and c_{IO}), while others are specific to the formulation of each setup. Details regarding P^* and C^* are provided in Eq. 1. R_I , R_S , and R_P are tuning parameters for the albedos of ice, snow, and melt ponds in the Delta-Eddington radiation scheme (Briegleb & Light, 2007). Note that δ_P , the constant ratio between the melt pond depth and melt pond fraction in the CESM melt pond parameterization, has been classified as radiation parameter (Tab. 1a) because the scheme describes only the radiation effects of melt ponds (Holland et al., 2012). The lead closing parameter H_0 determines the thickness of newly formed ice (Hibler, 1979). μ is a tuning parameter that acts on the empirical e-folding scale of ridges, whose ITD is well approximated by a negative exponential (Lipscomb et al., 2007; Hunke, 2010; Uotila et al., 2012). The ice-atmosphere drag coefficient c_{IA} has not been optimized following the results of Massonnet et al. (2014),

which show that optimizing the atmospheric drag is not necessary if P^* and c_{IO} are already optimized.

2.5 Observational products

The Green’s function optimization method is based on three types of monthly averaged satellite observations and their uncertainties: sea-ice concentration, thickness, and drift (Fig. 2). We employ the OSI SAF Global Sea Ice Concentration Climate Data Record v2.0 (EUMETSAT Ocean and Sea Ice Satellite Application Facility, 2017) for the period 2002–2015. The retrieval of this product is based on passive microwave data from the SSM/I (Special Sensor Microwave/Imager) and SSMIS (Special Sensor Microwave Imager/Sounder) sensors (Lavergne et al., 2019). The data are distributed on a polar stereographic 25km resolution grid, which is approximately the same resolution as our model in the Arctic.

Two complementary sea-ice thickness datasets are considered during the freezing season (October to April): the monthly northern hemisphere sea-ice thickness from Envisat (2002–2010; Hendricks et al. (2018b)) and from CryoSat-2 (2011–2015; Hendricks et al. (2018a)). The merged CryoSat-2/SMOS sea-ice thickness product has not been considered for the parameter optimization because we decided to prioritize the optimization of thick sea-ice regions over the marginal ice zone. The evolution of the thin ice cover is implicitly constrained by the parallel employment of sea-ice concentration observations during the optimization, which compensates, at least to some extent, for the exclusion of the SMOS observations from the optimization.

Following Sumata et al. (2019a), sea-ice drift data covering the whole seasonal cycle are obtained by combining three different pan-Arctic low-resolution products: the OSI-405 (Lavergne et al., 2010), the sea-ice motion estimate by Kimura et al. (2013), and the Polar Pathfinder Daily 25 km EASE-Grid Sea Ice Motion Vectors, Version 2 (NSIDC Drift hereafter; Tschudi et al. (2010); Fowler et al. (2013)). OSI-405 is the drift product with the smallest observational uncertainties (Sumata et al., 2014) and therefore, when possible, it is preferred to the others. The estimates by Kimura et al. (2013) are used in summer because the OSI-405 temporal coverage is limited to the winter months. The NSIDC Drift data are used to cover a gap left by the other two products during part of 2011 and 2012.

Additionally, the model simulations are compared to other types of sea-ice observations than those employed for the Green’s function optimization. As for the northern hemisphere,

(a) Optimized parameters in C1

Ocean albedo	α_O	Therm. conductivity snow	k_S
Dry sea-ice albedo	α_{Id}	H79 ice strength const.	P^*
Wet sea-ice albedo	α_{Iw}	H79 ice strength const.	C^*
Dry snow albedo	α_{Sd}	Ice-ocean drag	c_{IO}
Wet snow albedo	α_{Sw}	Lead closing param.	H_0

(b) Optimized parameters in C2

Ocean albedo	α_O	Therm. conductivity snow	k_S
Visible sea-ice albedo	α_{Iv}	H79 ice strength const.	P^*
Infrared sea-ice albedo	α_{Ii}	H79 ice strength const.	C^*
Visible snow albedo	α_{Sv}	Ice-ocean drag	c_{IO}
Infrared snow albedo	α_{Si}	Redistribution ridged ice	μ

(c) Optimized parameters in C3

Ocean albedo	α_O	Therm. conductivity snow	k_S
Sigma coeff. for ice albedo	R_I	H79 ice strength const.	P^*
Sigma coeff. for snow albedo	R_S	H79 ice strength const.	C^*
Sigma coeff. for pond albedo	R_P	Ice-ocean drag	c_{IO}
Melt pond shape	δ_P	Redistribution ridged ice	μ

Parameter types

Radiation	Sea-ice thermodynamics
Sea-ice thickness / ITD	Sea-ice dynamics

Table 1. Model parameters optimized for each of the three model configurations C1, C2, and C3. The division of the model parameters in four groups reflects the sea-ice model aspect regulated by the parameters. These groups are defined and color-coded as follows: radiation=blue, sea-ice thickness / ITD = gray, sea-ice thermodynamics=green, and sea-ice dynamics=red.

the southern hemisphere sea-ice concentration is taken from the OSI SAF Global Sea Ice Concentration Climate Data Record v2.0. Starting from 2016, we use the operational extension of the OSI-450, denominated OSI-430-b, for both hemispheres (EUMETSAT Ocean and Sea Ice Satellite Application Facility, 2019). The retrieval of snow depth on top of the sea ice is based on an empirical algorithm that uses passive microwave satellite observations from the AMSR-E (Advanced Microwave Scanning Radiometer; Rostosky et al. (2019b)) and AMSR-2 (Rostosky et al., 2019a) sensors, as described by Rostosky et al. (2018).

2.6 Cost Function

The optimization of the model parameter space leads to modifications of the sea-ice state and, consequently, to a variation of the cost function measuring the mismatch between model results and observations. Studying the cost function represents therefore a useful approach to assess changes in model performance taking the observational uncertainties into account. Before presenting the main findings of our study, we clarify some aspects related to the cost function formulation and interpretation. From a mathematical viewpoint, the cost function F (Eq. 9) employed in the assessment of the model performance is the same quadratic cost function that is minimized during the Green’s function parameter optimization (Eq. 5):

$$F = \frac{1}{N_o} \sum_{i=1}^{N_o} \frac{(y_i - x_i)^2}{\sigma_i^2}, \quad (9)$$

where y_i is a single observation with standard deviation σ_i , x_i is the corresponding model value, and N_o the total number of observations. In the context of model performance evaluation, F is computed separately for each observation type at different stages of the parameter optimization procedure (before optimization, after one iteration, and lastly after the second iteration). Assuming that the observations represent accurately the “true” state of the sea-ice cover, a change in cost function (Δ_F) can indicate an improvement ($\Delta_F < 0$) or degradation ($\Delta_F > 0$) of the model performance. Note that, due to the quadratic nature of the cost function, $F = 4$ indicates that, on average, the mismatch between model results and observations is equal to 2 ($= \sqrt{4}$) standard deviations of the observations.

Although the initial parameter values of different model setups before the optimization has been made as homogeneous as possible, the pre-optimization cost function values differ inevitably for each model configuration (Fig. 3). This behavior depends on multiple factors:

1. The intrinsic ability of a specific model formulation to reproduce the observed state.
2. The quality of the employed atmospheric forcing and its compatibility with each model formulation.
3. The “distance” of each pre-optimization parameter set from the optimized one (i.e. how well the model parameters are manually tuned already).

The relative contribution of these factors is difficult to quantify and can change substantially depending on the variable of interest (e.g. sea-ice concentration, thickness, etc.). An obvious consequence of point 3 is that a configuration far from its optimal state can be optimized more effectively than a configuration closer to it. For being able to evaluate more reasonably a property that we call the model “flexibility”—the extent to which a model configuration can be optimized for a variable—we propose a normalized version of Δ_F for each of the model variables and observations considered:

$$\|\Delta_F\| = \frac{\sqrt{F_f} - \sqrt{F_i}}{\sqrt{F_i}} \cdot \sqrt{\frac{\min\{F_i^{C1-E}, \dots, F_i^{C3-N}\}}{F_i}}, \quad (10)$$

where F_i and F_f are the cost function values respectively before and after the Green’s function parameter optimization. The square-roots in Eq. 10 are introduced as compensation for the quadratic nature of the cost function. In practice, the normalized formulation $\|\Delta_F\|$ (Fig. 3; gray percentages) has the effect of reducing the cost function change in those configurations that start further away from the optimal state before the optimization, providing a suitable metric for assessing the flexibility of the model configurations.

3 Results

3.1 Sea-ice concentration and position of the ice edge

The Green’s function parameter optimization improves the model representation of the sea-ice concentration for each of the six configurations considered (Fig. 3; top-left). The C3 setup performs better than C1 and C2 both under ERA5 and NCEP atmospheric forcing, suggesting that a more complex formulation of the sea-ice model is beneficial for simulating this appropriately variable. In the Icepak setups C2 and C3, the employment of the NCEP forcing leads to better results than ERA5 in terms of the absolute values of the cost function. In contrast, the cost function values of the optimized C1 configurations are comparable under ERA5 and NCEP forcing. Overall, the C1 setup shows higher flexibility, and it is capable of compensating more effectively for differences in boundary conditions.

Simulating correctly the sea-ice edge position is a requirement for every modern sea-ice model. Because the definition of the ice edge position is based on the sea-ice concentration, one might expect the parameter calibration technique based on sea-ice concentration observations to also improve the representation of this feature. This assumption is reasonable, with one caveat: the observational uncertainties of the sea-ice concentration are largest in the vicinity of the ice edge, slightly reducing the weight of these key regions on the total cost function and prioritizing the optimization of pack ice locations, where however the agreement between model and observations is generally already good. Here we analyze the correctness of the sea-ice edge position based on two metrics, the Integrated Ice Edge Error (IIEE), and the Absolute Extent Error (AEE; Goessling et al. (2016)), a component of the IIEE (Fig. 4). The AEE is defined as the absolute difference in sea-ice extent between model and observations. However, two different configurations of the sea-ice edge can lead to the same sea-ice extent, hence to an $AEE = 0$. The IIEE is designed to overcome this issue and penalizes situations where sea ice is misplaced in the model simulations compared to the observations.

In terms of IIEE and AEE, the ranking of the six optimized model configurations for the Arctic (Fig. 4; top row) confirms what emerges from the analysis of the sea-ice concentration cost function: the C3-N configuration performs best while the C2-E configuration performs worst, exhibiting an error peak in summer for both the IIEE and AEE. This error is caused by a strong sea-ice underestimation. Overall, the NCEP forcing leads to a better sea-ice edge representation than ERA5. In all the configurations, both the error magnitude and its variability are largest in late spring and in early summer, while lowest during the winter months. This might suggest a better representation in the model of the physical processes regulating the sea-ice freeze-up compared to those regulating its melting. Furthermore, the 2 m temperature transition across the sea-ice edge in the atmospheric forcing is much sharper during the freezing season than during the melting season, allowing little freedom to the sea-ice model where to place the sea-ice edge and leading to better winter performance. These features are also evident in Fig. 5, which draws a comparison between the sea-ice concentration of C3-N, the best configuration for this variable, and of the observations at different stages of the seasonal cycle. The results confirm the very good performance of C3-N, with just small deviations from the observations in terms of both the sea-ice concentration and sea-ice edge position, particularly evident in June in melting locations. However, the presence of melt ponds causes an underestimation of the observed sea-ice concentration

(Kern et al., 2016) and this could explain the excessive sea-ice concentration in the model along the coasts and in the marginal ice zone for the month of June.

The ice-edge position analysis has been repeated for the Southern Ocean (Fig. 4; bottom row), whose sea-ice observations have not been considered in the parameter optimization. The results evidence some similarities with the Arctic: the IIEE and AEE are largest during the melting season and lowest in winter when the sea-ice extent reaches its maximum. As for the Arctic, the six configurations exhibit a larger error spread during the summer months. The ranking of the model setups in terms of IIEE and AEE changes substantially in the hemispheres. In Antarctica, the C2 setup, which had the worst performance in the Arctic, exhibits the lowest IIEE and AEE from February to June, followed by the C3 and C1 setups. The situation is inverted from July to January when the differences among the model configurations are however much smaller. Overall, in the Southern Ocean, the Icepack setups C2 and C3 perform comparably or better (depending on the season considered) than the standard FESOM2 formulation C1.

3.2 Sea-ice thickness

The analysis of the sea-ice thickness cost function reveals similar performance of different model configurations (Fig. 3; bottom-left plot). The cost function values around 1 indicate that, on average, the mismatch between model results and observations is of the same magnitude as the observations uncertainties. After optimization, the model setup C1 exhibits slightly better performance than the C2 and C3 for both atmospheric forcings. Coincidentally, C1 is also the model setup that benefits more from the parameter optimization, with the C1-E and C1-N configurations showing respectively a $\sim -17\%$ and $\sim -20\%$ normalized cost function change. In contrast, the C3-N configuration, which ranks first before optimization, is negatively affected by the optimization and exhibits a $\sim 6\%$ normalized cost function increase.

The model simulations have been compared to three distinct sea-ice thickness observational products (Fig. 6): the Envisat and CryoSat-2 products, which target the thicker sea-ice ($>1\text{m}$) for different periods, and the merged CryoSat-2/SMOS product, which combines the capability of the SMOS sensor to detect thin sea-ice with the CryoSat-2 measurements in thicker regions. When compared to the observations, the performance of the model configurations changes slightly depending on the choice of the observational product. The

Envisat and CryoSat-2 comparison reveal a general underestimation of the average sea-ice thickness by all the model configurations (Fig. 6; upper and middle plot). To a certain extent, this underestimation is a consequence of the absence of essentially all thin sea-ice from these observational products, while the thin ice is still present in the model simulations and can be included in the average thickness computation if the spatial distribution of the sea-ice thickness is different in model simulations and observations. In contrast, the CryoSat-2/SMOS measurements provide a more complete picture of the sea-ice thickness up to the ice edge. It is therefore more compatible with the model results and allows a more robust comparison. Consequently, the agreement between this observational product and the model results is better (Fig. 6; bottom plot).

Overall, the sea-ice thickness discrepancies among the optimized model configurations are moderate: on average 25cm, and up to 60cm (Fig. 6). The average sea-ice thickness of different configurations tends to converge towards the end of the freezing season, while the spread is slightly larger at its beginning. The results evidence wider discrepancies in terms of model setups than in terms of the atmospheric forcing employed, with C1 having on average a thicker sea-ice cover than C3 and C2. All the model configurations represent fairly well the observed inter-annual variability and the seasonal cycle. For example, both the model simulations and the observations coherently indicate a relatively low sea-ice thickness over the periods 2012–2013 and 2016–2018, and relatively thick sea-ice in 2014–2015. Overall, the model performance in terms of sea-ice thickness is generally better than that of most of the global ocean–sea ice reanalyses from the Ocean Reanalyses Intercomparison Project (ORA-IP) analyzed by Uotila et al. (2019) and Chevallier et al. (2017). Note that most of the models analyzed in ORA-IP assimilate sea-ice concentration and/or sea-surface temperature, in addition to other non sea-ice variables.

3.3 Sea-ice drift

The sea-ice drift is the model variable for which the parameter optimization procedure is least successful, with a normalized cost function change of on average $\sim -1\%$, and for which the cost function values of different model configurations are most similar (Fig. 3; upper-right plot). This behavior can be explained by the fact that the formulation of the dynamic solver has an effect on the simulated sea-ice velocity at least as large (if not more) as the employment of different atmospheric boundary conditions, of sea-ice rheology, and of ice-ocean dynamical interactions (Losch et al., 2010). In this respect, all the model configura-

tions considered here share the same EVP solver for the sea-ice momentum equation, which constrains substantially the model behavior, and which cannot be calibrated through the optimization of model parameters. The remaining variability of model performance in terms of sea-ice drift appears to be linked to the choice of the atmospheric forcing. The sea-ice drift optimization is effective only for configurations running under the ERA5 atmospheric forcing, which features a cost function reduction. In contrast, the optimization impact on the configurations running under the NCEP forcing is very small. The poor sea-ice drift performance of C2-E is caused by the summer biases affecting the sea-ice concentration and thickness described in the previous sections.

The simulated sea-ice drift represents well the observed spatial features of the sea-ice circulation in the Arctic, as evidenced by the case study in Fig. 7. Here, we limit our analysis to a single month (April 2015) because averaging the sea-ice drift over multiple months and/or years could lead to the cancellation of compensating errors. The anticyclonic circulation in the Beaufort Sea is well represented, as well as the meandering transpolar drift, and the sea-ice export through Fram Strait and the Baffin Bay. The model drift fields are overall smoother and less detailed than the observed drift field. This is caused partially by the finite resolution of the atmospheric forcing and partially by shortcomings of the numerical implementations of the sea-ice model. A clear aspect that emerges from all the simulations is that the sea-ice in the model is generally slower than the observations, particularly where the drift is faster (e.g. coast of Alaska, Baffin Bay, and Kara Sea). This feature is also evident in Fig. 8, which is largely dominated by a positive bias. However, the ERA5 configurations tend to overestimate the speed of slow sea-ice ($\mathbf{v}_{ice} < \sim 5 \text{ cm s}^{-1}$), which results in a too strong sea-ice recirculation from the transpolar drift into the Beaufort gyre (Fig. 7). Such a feature is better captured by the NCEP configurations, whose levels of performance remain nevertheless worse than ERA5 over most of the Arctic domain.

3.4 Snow thickness

Although winter snow thickness observations have not been employed in the Green's function optimization procedure, the analysis of its cost function gives an interesting insight into the performance of the analyzed model configurations concerning this variable. Fig. 3 (bottom right plot) shows two distinct behaviors for the Icepack setups C2 and C3, and for the standard FESOM2 setup C1. The performance of the latter is worse than that of C2 and C3, before and after the parameter optimization procedure, and regardless of the

employed atmospheric forcing. At the same time, C1 is the only setup on which the Green's function optimization has a positive impact, suggesting again greater flexibility of this setup compared to the other two. The C1 snow thickness improvements are likely linked to a better-simulated sea-ice concentration, which presence is mandatory for the accumulation of the precipitated snow.

Discrepancies in snow precipitation between different atmospheric reanalysis can be due to the different atmospheric models, data assimilation techniques, and observations used for the production of the reanalysis. Barrett et al. (2020) show that this is also the case in the Arctic, where the snow precipitation is higher in the NCEP products compared to ERA5. In this respect, our results are in good agreement with the previous studies: the snow over sea ice in the ERA5 configurations is thinner than that in the NCEP configuration (Fig. 9; bottom row). Furthermore, the snow in the C1 setup is overall thicker than that in C2 and C3 for both forcing products (Fig. 9; right column). This is likely due to the ridging parameterization adopted in Icepack, which assumes that a fraction of the snow that participates in the ridging (50% in our setups) is lost in the ocean, where it melts eventually. A comparable snow sink is missing in the standard FESIM formulation, hence the thicker snow layer. The observed snow thickness lies in between the NCEP and ERA5 configurations of the C2 and C3 setups. These exhibit comparable cost function values, attributable however to model biases of opposite sign, positive for NCEP and negative for ERA5.

3.5 Optimized parameters

Fig. 10 compares five optimized parameters for the six model configurations analyzed here. Overall, differences in model formulation appear to have a larger impact on optimized parameter values than differences in atmospheric forcings. Some of the parameters vary more coherently than others. For example, the optimized ice-ocean drag c_{IO} values are systematically larger than in the control run, for all the setups. In this respect, our results are in good agreement with Sumata et al. (2019b), which finds an optimized c_{IO} value of 0.00847 for the NAOSIM model, but they differ from the optimal estimates of Ungermann et al. (2017) (0.00664 for the MITgcm model) and Massonnet et al. (2014) ([0.00294, 0.00378] for the NEMO-LIM3 model, also associated to a much lower value of P^* compared to our simulations). All the previously mentioned models run with the NCEP atmospheric forcing.

The calibration of P^* leads to minor parameter changes for the setups C1 and C3. In contrast, P^* is reduced in both configurations of the C2 setup. This parameter reduction is likely a consequence of the negative thickness and concentration biases of this setup, which is mitigated in part by reducing the sea-ice strength. A less stiff sea-ice cover leads to more ridging in winter and, in turn, to an increase of the sea-ice volume and extent. A similar consideration can be made for the relatively high values of C^* for the C2 configurations, which also concur with a reduction of the sea-ice strength. Only the C1-E configuration shows a pronounced reduction of C^* , which implies an increase of the sea ice strength in summer.

The ocean albedo exhibits two different types of behavior: $\alpha_O \approx 0.085$ for the Icepack setups while $\alpha_O \approx 0.042$ for the standard FESOM2 setup, a factor-two difference. Note that the treatment of the ocean albedo is equally simplistic in all the model setups considered (no dependency on the incident angle of solar radiation). Therefore, differences in model formulations with respect to this parameter cannot explain the dual behavior observed. Such a feature might be likely linked to different assumptions in the model implementation of the processes regulating the melting of sea ice, which is impacted by the ocean surface temperature and thus influenced by α_O . In particular, the presence of an ITD in C2 and C3 favors the complete sea-ice melting in thin ice categories, thus decreasing the sea-ice concentration. A higher α_O can limit an excessive melting and the consequent decrease in sea-ice concentration. Additionally, the Icepack configurations include a thermodynamic parameterization for lateral melting of ice floes that is also modulated indirectly by α_O similarly to the ITD. The effect of lateral melting on α_O is, however, smaller compared to that of the ITD. Note that α_O is the only parameter chosen for the calibration with a substantial impact on the global ocean rather than only on the polar regions. Although both values fall inside the admissible observational range (Jin et al., 2004), a choice in one or the other direction could impact and possibly degrade the model performance concerning the ocean temperatures outside the Arctic. Such a parameter should therefore be manipulated with extreme care, and it could be optimized much more effectively by constraining the optimization procedure with sea-surface temperature observations. Nevertheless, in uncoupled setups varying α_O has a limited effect on the simulated sea surface temperature because this variable is also constrained by the near surface temperature from the atmospheric forcing. Such an assumption does not hold in fully coupled setups, where a correct ocean albedo formulation becomes crucial.

Urrego-Blanco et al. (2016) describe the prime role of the snow thermal conductivity k_S in regulating the winter growth of sea-ice in the CICE model. A large k_S allows more heat transfer from the ocean to the atmosphere during winter, enhancing the bottom growth of sea ice and leading to a thicker sea-ice cover. The opposite is true for a low k_S . Apparently, the Green’s function parameter optimization effectively exploits this mechanism to reduce the sea-ice thickness biases in the model configurations (Fig. 3; bottom-left plot): the Icepack C2-E, C3-E, and C2-N configurations—negatively biased before the optimization—see an increase of k_S . The C1-E and C1-N configurations, both positively biased in snow and sea-ice thickness before the optimization, experience a reduction of k_S . C3-N, which before the optimization exhibits the best sea-ice thickness correspondence between model results and observations, is the configuration with the least k_S change.

4 Discussion

4.1 Considerations on the Green’s function optimization method

In Sec. 2.3, we argued that the linearization of the system in the Green’s function optimization is overall an appropriate approximation, even though the physics of the ocean/sea-ice system presents well-known nonlinearities. The validity of this assumption is non-trivial to prove mathematically. However, the fact that the application of the Green’s function approach leads to a cost function reduction, and that this reduction is generally less in a second iteration of the method, provides evidence that the optimization method works as expected, including the linearization assumption. Despite this, the fact that the Green’s function approach is a robust method for tuning the model effectively does not guarantee that the estimated optimal parameters lead to a model state that corresponds to a global minimum of the cost function, particularly when the cost function is not a “well-behaved” function as in the case of sea-ice. In this respect, the results by Sumata et al. (2013) show that a stochastic optimization method is more appropriate for finding a global minimum of the cost function than gradient descent methods as the Green’s function approach (Figs. 4 and 5 of Sumata et al. (2013) reveal the heterogeneity of the sea-ice concentration cost function). In the context of this study, where the model optimization is performed for three model configurations each forced with two sets of atmospheric boundary conditions, the Green’s function approach has been chosen because it provides a balance between the effectiveness of the method, simplicity of implementation, and associated computational costs.

4.2 Shortcomings of the parameter optimization

The first unsatisfactory outcome of the parameter optimizations regards the very weak sea-ice drift performance improvement (Sec. 3.3) compared to that of sea-ice concentration and thickness. We attempt to understand this behavior by performing an additional round of Green’s function optimization to C3-N, the best performing configuration presented in this study. The additional iteration features the ice-atmosphere drag coefficient c_{IA} among the optimized parameters, together with α_O , R_I , R_S , R_P , δ_P , k_S , P^* , C^* , and c_{IO} . The new optimization is performed in two flavors: a standard optimization that accounts for sea-ice concentration, thickness, and drift speed with equal weights (called C3-N-a), and a more dynamically oriented optimization where the only observations considered is the sea-ice drift (called C3-N-b). In both cases, the optimal parameter perturbations resulting from the Green’s function optimization are small and do not bring substantial improvements to the sea-ice drift performance, which remains comparable to the control simulation (C3-N-control; Fig. 11). In this respect, our results agree with Massonnet et al. (2014), who indicate that the optimization of P^* and c_{IO} is sufficient for constraining the sea-ice drift. In our study, the optimization of c_{IA} in addition to P^* and c_{IO} does not improve the model performance compared to the optimization of P^* and c_{IO} alone. This evidence suggests that the sea-ice drift optimization reached a limit with respect to our model setup, optimization method, and observations and forcing employed. As a consequence of a slower sea-ice drift in our simulations, an over-optimization of thermodynamic and radiative processes (e.g. enhanced formation of new sea-ice or reduced melting) might have occurred to compensate for the reduced sea-ice transport outside the Arctic. Nonetheless, the reader should note that the sea-ice drift performance of our model configurations are overall good and in line with those of other sea-ice and ocean models with data assimilation (e.g. Massonnet et al. (2014); Chevallier et al. (2017)).

A second aspect that deserves some discussion concerns the overall poor performance of the C2 model setup, and particularly of C2-E. This configuration exhibits a strong negative bias in sea-ice concentration and thickness during summer, which consequently impacts the model performance also in terms of sea-ice drift and snow thickness. This bias likely results from a misrepresentation of the sea-ice radiative processes in the model and, once more, it might be due to an unwise choice concerning the parameters for the optimization. The C2 setup employs the CCSM3 radiation scheme, in which, as described in Sec. 2.2, the sea-ice and snow albedo values are split into a visible and an infrared component with a thickness

and temperature dependence. These four albedo values have been optimized in the present study (Tab. 1). However, the model parameters that regulate the thickness and temperature dependence of the albedo have not been optimized, leading to a poor representation of the melting processes. We observe that both the simpler radiation scheme employed in C1 and the complex delta-Eddington radiation formulation used in C3 respond to the parameter optimization better than the CCSM3 scheme, but for different reasons. On one hand, the radiation scheme in C1, in principle similar to that in C2 but less sophisticated, can be likely tuned more effectively because dependent on fewer model parameters. On the other hand, the radiation scheme in C3, which is more sophisticated than C2, responds better to the model tuning because the non-optimized parameters are already better constrained and more physically based.

4.3 Computational costs

The increased complexity of the FESOM2 extended sea-ice model comes with a non-negligible price in terms of computational costs. Fig. 12 shows that the sea-ice computations of the Icepack setups C2 and C3 are approximately four times slower than C1, the simpler standard FESOM2 setup. This behavior was expected and caused partially by the more detailed formulation of Icepack thermodynamics, but primarily by the growing number of tracers needed to describe the sea-ice state. These tracers need to be advected separately by the FE-FCT scheme, which translates into a linear increase of the cost for each additional tracer. Furthermore, a set of tests has been implemented to guarantee the conservation of enthalpy, freshwater, and salinity during the advection process, which further increases the computational requirements. An incremental remapping scheme for the advection of sea-ice tracers similar to that implemented in CICE (Lipscomb & Hunke, 2004), which is conservative and becomes very efficient when the number of tracers is large, will be considered in the future for further reducing the computational cost of the FESOM2-Icepack.

Nevertheless, running FESOM2 with Icepack remains feasible, and represents a viable option for future modeling studies with a focus on polar regions. The mesh employed for this study is designed with most of the surface nodes in sea-ice active regions, causing the sea-ice computations to account for a substantial part of the model budget, and thus constituting a rather extreme case if compared to CMIP-type applications. The relative cost of the Icepack computations will be lower in meshes with most of the nodes in non-sea-ice regions. Furthermore, in high-resolution simulations (1km to 4km), the contribution of the

EVP solver is expected to become predominant over the advection of tracers, due to the increasing number of sub-cycles needed for reaching a converging solution of the momentum equation. An in-depth investigation of the computing performance of the FESOM2-Icepack model for a broader range of scenarios will be the topic of a future study.

4.4 Future prospects for the sea-ice representation in FESOM2

As described in Sec. 2.2, the options offered by Icepack in terms of sea-ice physics go beyond those explored in this study. In particular, future work will focus on the impact of a highly resolved ITD on the simulated sea-ice thickness and drift (also at high spatial resolution using the metrics developed by Hutter et al. (2019)), on the exploration of the floe-size distribution parameterizations, and on the investigation of the sophisticated "mushy layer" thermodynamics (A. K. Turner et al., 2013), which has not been considered in this study. Future FESOM2-Icepack model simulations could also serve as boundary conditions for detailed single-column studies with Icepack in a Lagrangian framework (e.g. Krumpen et al. (2020)), allowing to retain a high physical consistency between the driving model and the single-column model.

Most of the model configurations here analyzed show a minimum in AEE in July (Fig. 4; top right), suggesting that the IIEE is mostly caused by sea-ice misplacement rather than by a wrong representation of the sea-ice extent. This behavior could in part reflect the fact that our model cannot simulate the processes leading to land-fast sea-ice formation, both in its standard formulation and with Icepack. The absence of this persistent sea-ice type impacts the detachment location of the pack ice from the Arctic coastline and in turn the correctness of the sea-ice edge position for this month. Model formulations that enable, to a certain extent, the simulation of land-fast sea ice in shallow seas already exist (Lemieux et al., 2015, 2016) and proved to be effective in the CICE and MITgcm models. Therefore, they will be considered for future versions of the FESOM2 model.

The FESOM sea-ice and ocean model plays a central role in the climate modeling and forecasting activities at the Alfred Wegener Institute (AWI), and is included in different versions of the CMIP6 AWI Climate Model (AWI-CM; Sidorenko et al. (2015); Rackow et al. (2016); Sidorenko et al. (2019); Semmler et al. (2020)). In this respect, we plan to couple the new FESOM2-Icepack setup to the latest climate model configuration under development at AWI, which uses the open-source version of the Integrated Forecast System

(OpenIFS) as the atmospheric model. The availability of a more detailed sea-ice description in a fully coupled setup will enable a better understanding of the interactions between a warming atmosphere and sea ice. At the same time, the new coupled configuration will allow us to perform sea ice-oriented climate modeling studies (e.g. Zampieri & Goessling (2019)) under more physically consistent assumptions. Finally, FESOM2-Icepack will be integrated in the Seamless Sea Ice Prediction System (SSIPS; Mu et al. (2020)) and thus equipped with the Parallel Data Assimilation Framework (PDAF; (Nerger & Hiller, 2013)) for assimilating ocean and sea-ice observations with an Ensemble Kalman Filter.

5 Summary and conclusions

This study presented a new formulation of the sea-ice component of the unstructured-mesh FESOM2 model. The update, which exploits the state-of-the-art capabilities of the sea-ice single-column model Icepack, improves the physical description of numerous sea-ice sub-grid processes while retaining a modular structure that enables the user to adapt the sophistication of the sea-ice model formulation to the requirements of a specific investigation. Because of this modularity, the new FESOM2 formulation enables investigation of the impact of the sea-ice model complexity on the performance of the sea-ice simulations under two different atmospheric forcings.

Our findings indicate that the sophisticated C3 setup performs systematically better than C2 and C1 concerning the Arctic sea-ice concentration and snow thickness, supporting the hypothesis that an elaborated model formulation leads to a more appropriate representation of the sea ice. However, the results also indicate that the setup ranking that emerges for the sea-ice concentration in the Arctic does not hold in the Southern Ocean, which has not been included in the optimization; here the C2 setups perform best. The current generation of atmospheric forcings and sea-ice/ocean models is therefore still not fully balanced and fails to guarantee an adequate representation of the sea ice in both hemispheres simultaneously. For other variables, model complexity appears to play only a marginal role in defining the quality of sea-ice simulations. This is the case for sea-ice thickness and drift, for which the differences between the various FESOM2 configurations are small and independent of model sophistication. We argue that the motivations behind this are different for the two variables. On one hand, sea-ice thickness is the integrated result of multiple dynamic and thermodynamic model processes, including possible compensating effects. Therefore, the complexity of the sea-ice sub-grid processes is less relevant and the Green's function

approach is only effective for first-order processes that affect the thickness, such as changes in snow conductivity. The lack of response of the sea-ice drift, on the other hand, can be due to the fact that the EVP implementation introduces, to a certain extent, a stochastic behavior into the model, with the end result that the sea-ice dynamics is almost entirely constrained by the atmosphere and ocean forcings, except for some deceleration where the sea-ice strength is high. Sub-grid processes with varying sophistication do not influence the drift particularly because, in the model configuration here investigated, the solver of the momentum equation is not aware of the sea-ice sub-grid state (all the configurations employ the H79 strength formulation). Finally, we find that the simple C1 setup responds better to the optimization procedure, showing larger improvements compared to C2 and C3, and thus suggesting that a less complex model can be tuned more effectively.

In addition to the model formulation, the choice of the atmospheric forcing product substantially influences the sea-ice simulations. Concerning the sea-ice concentration, the Icepack setups C1 and C2 perform much better when forced with the NCEP product compared to ERA5, both in the Arctic and in the Antarctic. The C1 setup exhibits similar results for NCEP and ERA5 in the Arctic, while the NCEP forcing outperforms ERA5 in the Antarctic. The opposite is true for the sea-ice drift and the snow thickness variables, which benefit from the employment of the ERA5 product instead of NCEP. In summary, both the atmospheric forcing products here analyzed have strengths and weaknesses that should be considered when employing them to force sea-ice and ocean simulations.

The results of this study are valid for sea-ice/ocean only simulations, where the atmospheric conditions are prescribed from reanalysis products. Some of the findings might not hold in a fully coupled framework, where the atmosphere responds both thermodynamically and dynamically to sea-ice and ocean changes. A similar study could be implemented in a fully coupled configuration by optimizing the climatological sea-ice state of the model using the observational climatology as constraint. We plan to perform such a study for our modeling framework once the FESOM2-Icepack setup is coupled to the OpenIFS atmospheric model.

We conclude by underlining, once more, the importance of the semiautomatic parameter calibration for this study. Without the two cycles of Green's function optimization, our results would have conveyed a rather different message, erroneously indicating that the Icepack configurations perform systematically better than the standard FESOM2 model for

most of the variables considered (Fig. 3; large circles). The systematic optimization of the sea-ice parameters is certainly a time-consuming operation that requires a non-negligible amount of computing resources. Nevertheless, we recommend this approach, in some form, in future studies that aim to assess advances in the field of sea-ice modeling to guarantee a fair evaluation of sea-ice models.

6 Data availability statement

All the observational and forcing datasets used to force, validate, and optimize our model simulations are freely available. The exact address and the publisher associated to each dataset are referenced in Sec. 2.5 and 2.4. The simulation results and computational mesh are stored on Zenodo (Zampieri et al., 2020) and are publicly available. The Icepack source code, including instructions for compiling and running the model, can be downloaded from Zenodo (Hunke et al., 2020b).

Acknowledgments

L.Z., J.F., and H.F.G. acknowledge the financial support by the Federal Ministry of Education and Research of Germany (BMBF) in the framework of SSIP (grant 01LN1701A). L.Z. also acknowledges the funding from the European Union’s Horizon 2020 Research and Innovation program project APPLICATE (grant 727862). ECH acknowledges support from the Energy Exascale Earth System Modeling (E3SM) project of the US Department of Energy’s Office of Science, Biological and Environmental Research division. Furthermore, we are grateful to the German Climate Computing Centre (DKRZ) for granting computational resources through the BMBF computing project ”Impact of sea ice parameterizations on polar predictions”. We are very grateful to the CICE Consortium for creating and maintaining the Icepack sea-ice column physics package, as well as to the numerous scientists that over the years contributed to the development of the physical parameterization collected in this model. We thank Martin Losch and Sergey Danilov for the very helpful discussions that contributed to shaping this study. Furthermore, we also thank the OSI-SAF Consortium, the University of Bremen, and the NSIDC for making their sea ice observational products freely available.

References

- Barrett, A. P., Stroeve, J. C., & Serreze, M. C. (2020). Arctic ocean precipitation from atmospheric reanalyses and comparisons with north pole drifting station records. *Journal of Geophysical Research: Oceans*, 125(1), e2019JC015415. Retrieved from <https://agupubs.onlinelibrary.wiley.com/doi/abs/10.1029/2019JC015415> doi: 10.1029/2019JC015415
- Batrak, Y., & Müller, M. (2019). On the warm bias in atmospheric reanalyses induced by the missing snow over Arctic sea-ice. *Nature Communications*, 10(1), 4170. Retrieved from <https://doi.org/10.1038/s41467-019-11975-3> doi: 10.1038/s41467-019-11975-3
- Bitz, C. M., Fyfe, J. C., & Flato, G. M. (2002). Sea ice response to wind forcing from amip models. *Journal of Climate*, 15(5), 522 - 536. Retrieved from https://journals.ametsoc.org/view/journals/clim/15/5/1520-0442_2002_015_0522_sirtwf_2.0.co_2.xml doi: 10.1175/1520-0442(2002)015<0522:SIRTWF>2.0.CO;2
- Bitz, C. M., Holland, M. M., Weaver, A. J., & Eby, M. (2001). Simulating the ice-thickness distribution in a coupled climate model. *Journal of Geophysical Research: Oceans*, 106(C2), 2441-2463. Retrieved from <https://agupubs.onlinelibrary.wiley.com/doi/abs/10.1029/1999JC000113> doi: 10.1029/1999JC000113
- Bitz, C. M., & Lipscomb, W. H. (1999). An energy-conserving thermodynamic model of sea ice. *Journal of Geophysical Research: Oceans*, 104(C7), 15669-15677. Retrieved from <https://agupubs.onlinelibrary.wiley.com/doi/abs/10.1029/1999JC900100> doi: 10.1029/1999JC900100
- Blockley, E., Vancoppenolle, M., Hunke, E., Bitz, C., Feltham, D., Lemieux, J.-F., ... Schroeder, D. (2020). The Future of Sea Ice Modeling: Where Do We Go from Here? *Bulletin of the American Meteorological Society*, 101(8), E1304-E1311. Retrieved from <https://doi.org/10.1175/BAMS-D-20-0073.1> doi: 10.1175/BAMS-D-20-0073.1
- Briegleb, B. P., & Light, B. (2007). A delta-eddington multiple scattering parameterization for solar radiation in the sea ice component of the community climate system model. *NCAR Tech. Note TN-472+STR*, 100 pp. Retrieved from <https://opensky.ucar.edu/islandora/object/technotes%3A484/datastream/PDF/view>
- Chevallier, M., Smith, G. C., Dupont, F., Lemieux, J.-F., Forget, G., Fujii, Y., ... Wang, X. (2017). Intercomparison of the Arctic sea ice cover in global ocean-sea ice reanalyses from the ORA-IP project. *Climate Dynamics*, 49(3), 1107-1136. Retrieved from <https://>

- doi.org/10.1007/s00382-016-2985-y doi: 10.1007/s00382-016-2985-y
- Collins, W. D., Bitz, C. M., Blackmon, M. L., Bonan, G. B., Bretherton, C. S., Carton, J. A.,
... Smith, R. D. (2006). The community climate system model version 3 (ccsm3). *Journal
of Climate*, 19(11), 2122 - 2143. Retrieved from [https://journals.ametsoc.org/view/
journals/clim/19/11/jcli3761.1.xml](https://journals.ametsoc.org/view/journals/clim/19/11/jcli3761.1.xml) doi: 10.1175/JCLI3761.1
- Cooley, S. W., Ryan, J. C., Smith, L. C., Horvat, C., Pearson, B., Dale, B., & Lynch,
A. H. (2020). Coldest Canadian Arctic communities face greatest reductions in shorefast
sea ice. *Nature Climate Change*, 10(6), 533–538. Retrieved from [https://doi.org/
10.1038/s41558-020-0757-5](https://doi.org/10.1038/s41558-020-0757-5) doi: 10.1038/s41558-020-0757-5
- Danilov, S., Sidorenko, D., Wang, Q., & Jung, T. (2017). The Finite-volume Sea
ice–Ocean Model (FESOM2). *Geoscientific Model Development*, 10(2), 765–789. Re-
trieved from <https://gmd.copernicus.org/articles/10/765/2017/> doi: 10.5194/
gmd-10-765-2017
- Danilov, S., Wang, Q., Timmermann, R., Iakovlev, N., Sidorenko, D., Kimmritz, M., ...
Schröter, J. (2015). Finite-Element Sea Ice Model (FESIM), version 2. *Geoscientific
Model Development*, 8(6), 1747–1761. Retrieved from [https://gmd.copernicus.org/
articles/8/1747/2015/](https://gmd.copernicus.org/articles/8/1747/2015/) doi: 10.5194/gmd-8-1747-2015
- Dieckmann, G. S., & Hellmer, H. H. (2010). The importance of sea ice: An overview. In *Sea
ice* (p. 1-22). John Wiley Sons, Ltd. Retrieved from [https://onlinelibrary.wiley
.com/doi/abs/10.1002/9781444317145.ch1](https://onlinelibrary.wiley.com/doi/abs/10.1002/9781444317145.ch1) doi: 10.1002/9781444317145.ch1
- Döscher, R., Vihma, T., & Maksimovich, E. (2014). Recent advances in understanding the
arctic climate system state and change from a sea ice perspective: a review. *Atmospheric
Chemistry and Physics*, 14(24), 13571–13600. Retrieved from [https://acp.copernicus
.org/articles/14/13571/2014/](https://acp.copernicus.org/articles/14/13571/2014/) doi: 10.5194/acp-14-13571-2014
- EUMETSAT Ocean and Sea Ice Satellite Application Facility. (2017). *Global sea ice con-
centration climate data record 1979-2015 (v2.0)* [data set]. Norwegian and Danish Mete-
orological Institutes. Retrieved from [https://navigator.eumetsat.int/product/E0:
EUM:DAT:MULT:OSI-450](https://navigator.eumetsat.int/product/E0:EUM:DAT:MULT:OSI-450) doi: 10.15770/EUM_SAF_OSI_0008
- EUMETSAT Ocean and Sea Ice Satellite Application Facility. (2019). *Global sea ice concen-
tration interim climate data record 2016 onwards (v2.0)* [data set]. Norwegian and Dan-
ish Meteorological Institutes. Retrieved from [http://www.osi-saf.org/?q=content/
global-sea-ice-concentration-interim-climate-data-record-release-2](http://www.osi-saf.org/?q=content/global-sea-ice-concentration-interim-climate-data-record-release-2)
- Flocco, D., Feltham, D. L., & Turner, A. K. (2010). Incorporation of a physically based

- 878 melt pond scheme into the sea ice component of a climate model. *Journal of Geophys-*
 879 *ical Research: Oceans*, 115, C08012. Retrieved from <https://agupubs.onlinelibrary>
 880 [.wiley.com/doi/abs/10.1029/2009JC005568](https://agupubs.onlinelibrary.wiley.com/doi/abs/10.1029/2009JC005568) doi: 10.1029/2009JC005568
- 881 Flocco, D., Schroeder, D., Feltham, D. L., & Hunke, E. C. (2012). Impact of melt ponds on
 882 arctic sea ice simulations from 1990 to 2007. *Journal of Geophysical Research: Oceans*,
 883 117(C9). doi: 10.1029/2012JC008195
- 884 Fowler, C., Maslanik, J., Emery, W., & Tschudi, M. (2013). *Polar Pathfinder Daily*
 885 *25 km EASE-Grid Sea Ice Motion Vectors, Version 2 (daily and mean gridded field)*
 886 [data set]. NASA DAAC, National Snow and Ice Data Center, Boulder, CO. Retrieved
 887 2020-07-06, from <https://nsidc.org/data/NSIDC-0116/versions/2> doi: 10.5067/
 888 LHAKY495NL2T
- 889 Goessling, H. F., Tietsche, S., Day, J. J., Hawkins, E., & Jung, T. (2016). Predictability of
 890 the arctic sea ice edge. *Geophysical Research Letters*, 43(4), 1642-1650. Retrieved from
 891 <https://agupubs.onlinelibrary.wiley.com/doi/abs/10.1002/2015GL067232> doi:
 892 10.1002/2015GL067232
- 893 Hendricks, S., Paul, S., & Rinne, E. (2018a). *ESA Sea Ice Climate Change Initiative*
 894 *(Sea_Ice_cci): Northern hemisphere sea ice thickness from the CryoSat-2 satellite on a*
 895 *monthly grid (L3C), v2.0* [data set]. Centre for Environmental Data Analysis. Re-
 896 trieved from <http://dx.doi.org/10.5285/ff79d140824f42dd92b204b4f1e9e7c2> doi:
 897 10.5285/ff79d140824f42dd92b204b4f1e9e7c2
- 898 Hendricks, S., Paul, S., & Rinne, E. (2018b). *ESA Sea Ice Climate Change Initia-*
 899 *tive (Sea_Ice_cci): Northern hemisphere sea ice thickness from the Envisat satellite on*
 900 *a monthly grid (L3C), v2.0* [data set]. Centre for Environmental Data Analysis. Re-
 901 trieved from <http://dx.doi.org/10.5285/f4c34f4f0f1d4d0da06d771f6972f180> doi:
 902 10.5285/f4c34f4f0f1d4d0da06d771f6972f180
- 903 Hersbach, H., Bell, B., Berrisford, P., Hirahara, S., Horányi, A., Muñoz-Sabater, J., ...
 904 Thépaut, J.-N. (2020). The ERA5 global reanalysis. *Quarterly Journal of the Royal*
 905 *Meteorological Society*, n/a(n/a). Retrieved from <https://rmets.onlinelibrary.wiley>
 906 [.com/doi/abs/10.1002/qj.3803](https://rmets.onlinelibrary.wiley.com/doi/abs/10.1002/qj.3803) doi: 10.1002/qj.3803
- 907 Hibler, I., W. D. (1979). A Dynamic Thermodynamic Sea Ice Model. *Journal of*
 908 *Physical Oceanography*, 9(4), 815-846. Retrieved from [https://doi.org/10.1175/](https://doi.org/10.1175/1520-0485(1979)009<0815:ADTSIM>2.0.CO;2)
 909 [1520-0485\(1979\)009<0815:ADTSIM>2.0.CO;2](https://doi.org/10.1175/1520-0485(1979)009<0815:ADTSIM>2.0.CO;2) doi: 10.1175/1520-0485(1979)009<0815:
 910 ADTSIM>2.0.CO;2

- Holland, M. M., Bailey, D. A., Briegleb, B. P., Light, B., & Hunke, E. C. (2012). Improved Sea Ice Shortwave Radiation Physics in CCSM4: The Impact of Melt Ponds and Aerosols on Arctic Sea Ice. *Journal of Climate*, 25(5), 1413-1430. Retrieved from <https://doi.org/10.1175/JCLI-D-11-00078.1> doi: 10.1175/JCLI-D-11-00078.1
- Hunke, E. C. (2010). Thickness sensitivities in the cice sea ice model. *Ocean Modelling*, 34(3), 137 - 149. Retrieved from <http://www.sciencedirect.com/science/article/pii/S146350031000079X> doi: <https://doi.org/10.1016/j.ocemod.2010.05.004>
- Hunke, E. C., Allard, R., Bailey, D. A., Blain, P., Craig, A., Dupont, F., ... Winton, M. (2020a). CICE-Consortium/CICE: CICE Version 6.1.2 (Version 6.1.2). *Zenodo*. Retrieved from <https://zenodo.org/record/3888653#.XvsK1fJS9TY> doi: doi.org/10.5281/zenodo.3888653
- Hunke, E. C., Allard, R., Bailey, D. A., Blain, P., Craig, A., Dupont, F., ... Winton, M. (2020b). CICE-Consortium/Icepack: Icepack 1.2.1 (Version 1.2.1). *Zenodo*. Retrieved from <https://zenodo.org/record/3712299#.Xvn3DPJS9TZ> doi: doi.org/10.5281/zenodo.3712299
- Hunke, E. C., & Dukowicz, J. K. (1997). An Elastic-Viscous-Plastic Model for Sea Ice Dynamics. *Journal of Physical Oceanography*, 27(9), 1849-1867. Retrieved from [https://doi.org/10.1175/1520-0485\(1997\)027<1849:AEVPMF>2.0.CO;2](https://doi.org/10.1175/1520-0485(1997)027<1849:AEVPMF>2.0.CO;2) doi: 10.1175/1520-0485(1997)027(1849:AEVPMF)2.0.CO;2
- Hunke, E. C., Hebert, D. A., & Lecomte, O. (2013). Level-ice melt ponds in the Los Alamos sea ice model, CICE. *Ocean Modelling*, 71, 24-42. Retrieved from <https://www.sciencedirect.com/science/article/abs/pii/S1463500312001680?via%3Dihub> doi: 10.1016/j.ocemod.2012.11.008
- Hunke, E. C., Lipscomb, W. H., & Turner, A. K. (2010). Sea-ice models for climate study: retrospective and new directions. *Journal of Glaciology*, 56(200), 1162-1172. doi: 10.3189/002214311796406095
- Hutter, N., Zampieri, L., & Losch, M. (2019). Leads and ridges in arctic sea ice from rgps data and a new tracking algorithm. *The Cryosphere*, 13(2), 627-645. Retrieved from <https://tc.copernicus.org/articles/13/627/2019/> doi: 10.5194/tc-13-627-2019
- Jahn, A., Sterling, K., Holland, M. M., Kay, J. E., Maslanik, J. A., Bitz, C. M., ... Pollak, D. A. (2012). Late-twentieth-century simulation of arctic sea ice and ocean properties in the ccsm4. *Journal of Climate*, 25(5), 1431 - 1452. Retrieved from <https://journals.ametsoc.org/view/journals/clim/25/5/jcli-d-11-00201.1.xml> doi: 10

- 944 .1175/JCLI-D-11-00201.1
- 945 Jin, Z., Charlock, T. P., Smith Jr., W. L., & Rutledge, K. (2004). A parameterization of
 946 ocean surface albedo. *Geophysical Research Letters*, 31(22). Retrieved from [https://](https://agupubs.onlinelibrary.wiley.com/doi/abs/10.1029/2004GL021180)
 947 [agupubs.onlinelibrary.wiley.com/doi/abs/10.1029/](https://agupubs.onlinelibrary.wiley.com/doi/abs/10.1029/2004GL021180) doi: 10.1029/
 948 2004GL021180
- 949 Jordan, R. E., Andreas, E. L., & Makshtas, A. P. (1999). Heat budget of snow-covered
 950 sea ice at north pole 4. *Journal of Geophysical Research: Oceans*, 104(C4), 7785-
 951 7806. Retrieved from [https://agupubs.onlinelibrary.wiley.com/doi/abs/10.1029/](https://agupubs.onlinelibrary.wiley.com/doi/abs/10.1029/1999JC900011)
 952 1999JC900011 doi: 10.1029/1999JC900011
- 953 Kern, S., Rösel, A., Pedersen, L. T., Ivanova, N., Saldo, R., & Tonboe, R. T. (2016).
 954 The impact of melt ponds on summertime microwave brightness temperatures and
 955 sea-ice concentrations. *The Cryosphere*, 10(5), 2217–2239. Retrieved from [https://](https://tc.copernicus.org/articles/10/2217/2016/)
 956 tc.copernicus.org/articles/10/2217/2016/ doi: 10.5194/tc-10-2217-2016
- 957 Kimmritz, M., Danilov, S., & Losch, M. (2015). On the convergence of the modified
 958 elastic–viscous–plastic method for solving the sea ice momentum equation. *Journal of*
 959 *Computational Physics*, 296, 90–100. Retrieved from [https://www.sciencedirect.com/](https://www.sciencedirect.com/science/article/pii/S0021999115003083)
 960 [science/article/pii/S0021999115003083](https://www.sciencedirect.com/science/article/pii/S0021999115003083) doi: 10.1016/j.jcp.2015.04.051
- 961 Kimmritz, M., Danilov, S., & Losch, M. (2016). The adaptive EVP method
 962 for solving the sea ice momentum equation. *Ocean Modelling*, 101, 59–
 963 67. Retrieved from [https://www.sciencedirect.com/science/article/abs/pii/](https://www.sciencedirect.com/science/article/abs/pii/S1463500316300038?via%3Dihub)
 964 [S1463500316300038?via%3Dihub](https://www.sciencedirect.com/science/article/abs/pii/S1463500316300038?via%3Dihub) doi: 10.1016/j.ocemod.2016.03.004
- 965 Kimura, N., Nishimura, A., Tanaka, Y., & Yamaguchi, H. (2013). Influence of winter sea-ice
 966 motion on summer ice cover in the Arctic. *Polar Research*, 32. Retrieved from [https://](https://polarresearch.net/index.php/polar/article/view/3087)
 967 polarresearch.net/index.php/polar/article/view/3087 doi: 10.3402/polar.v32i0
 968 .20193
- 969 Krumpfen, T., Birrien, F., Kauker, F., Rackow, T., von Albedyll, L., Angelopoulos, M., ...
 970 Watkins, D. (2020). The MOSAiC ice floe: sediment-laden survivor from the Siberian
 971 shelf. *The Cryosphere*, 14(7), 2173–2187. Retrieved from [https://tc.copernicus.org/](https://tc.copernicus.org/articles/14/2173/2020/)
 972 [articles/14/2173/2020/](https://tc.copernicus.org/articles/14/2173/2020/) doi: 10.5194/tc-14-2173-2020
- 973 Kuzmin, D. (2009). Explicit and implicit FEM-FCT algorithms with flux lineariza-
 974 tion. *Journal of Computational Physics*, 8(7), 2517–2534. Retrieved from [https://](https://www.sciencedirect.com/science/article/pii/S0021999108006475)
 975 www.sciencedirect.com/science/article/pii/S0021999108006475 doi: 10.1016/
 976 j.jcp.2008.12.011

- 977 Lavergne, T., Eastwood, S., Teffah, Z., Schyberg, H., & Breivik, L.-A. (2010). Sea ice
978 motion from low-resolution satellite sensors: An alternative method and its validation
979 in the Arctic. *Journal of Geophysical Research: Oceans*, 115, C10032. Retrieved from
980 <https://agupubs.onlinelibrary.wiley.com/doi/abs/10.1029/2009JC005958> doi:
981 10.1029/2009JC005958
- 982 Lavergne, T., Sørensen, A. M., Kern, S., Tonboe, R., Notz, D., Aaboe, S., ... Pedersen, L. T.
983 (2019). Version 2 of the EUMETSAT OSI SAF and ESA CCI sea-ice concentration climate
984 data records. *The Cryosphere*, 13(1), 49–78. Retrieved from [https://tc.copernicus](https://tc.copernicus.org/articles/13/49/2019/)
985 [.org/articles/13/49/2019/](https://tc.copernicus.org/articles/13/49/2019/) doi: 10.5194/tc-13-49-2019
- 986 Lemieux, J.-F., Dupont, F., Blain, P., Roy, F., Smith, G. C., & Flato, G. M. (2016).
987 Improving the simulation of landfast ice by combining tensile strength and a parame-
988 terization for grounded ridges. *Journal of Geophysical Research: Oceans*, 121(10), 7354-
989 7368. Retrieved from [https://agupubs.onlinelibrary.wiley.com/doi/abs/10.1002/](https://agupubs.onlinelibrary.wiley.com/doi/abs/10.1002/2016JC012006)
990 [2016JC012006](https://agupubs.onlinelibrary.wiley.com/doi/abs/10.1002/2016JC012006) doi: 10.1002/2016JC012006
- 991 Lemieux, J.-F., Tremblay, L. B., Dupont, F., Plante, M., Smith, G. C., & Dumont, D.
992 (2015). A basal stress parameterization for modeling landfast ice. *Journal of Geophysical*
993 *Research: Oceans*, 120(4), 3157-3173. Retrieved from [https://agupubs.onlinelibrary](https://agupubs.onlinelibrary.wiley.com/doi/abs/10.1002/2014JC010678)
994 [.wiley.com/doi/abs/10.1002/2014JC010678](https://agupubs.onlinelibrary.wiley.com/doi/abs/10.1002/2014JC010678) doi: 10.1002/2014JC010678
- 995 Lipscomb, W. H., & Hunke, E. C. (2004). Modeling Sea Ice Transport Using Incremental
996 Remapping. *Monthly Weather Review*, 132(6), 1341-1354. Retrieved from [https://](https://doi.org/10.1175/1520-0493(2004)132<1341:MSITUI>2.0.CO;2)
997 [doi.org/10.1175/1520-0493\(2004\)132<1341:MSITUI>2.0.CO;2](https://doi.org/10.1175/1520-0493(2004)132<1341:MSITUI>2.0.CO;2) doi: 10.1175/1520
998 -0493(2004)132<1341:MSITUI>2.0.CO;2
- 999 Lipscomb, W. H., Hunke, E. C., Maslowski, W., & Jakacki, J. (2007). Ridging, strength,
1000 and stability in high-resolution sea ice models. *Journal of Geophysical Research: Oceans*,
1001 112, C03S91. Retrieved from [https://agupubs.onlinelibrary.wiley.com/doi/abs/](https://agupubs.onlinelibrary.wiley.com/doi/abs/10.1029/2005JC003355)
1002 [10.1029/2005JC003355](https://agupubs.onlinelibrary.wiley.com/doi/abs/10.1029/2005JC003355) doi: 10.1029/2005JC003355
- 1003 Losch, M., Menemenlis, D., Campin, J.-M., Heimbach, P., & Hill, C. (2010). On
1004 the formulation of sea-ice models. part 1: Effects of different solver implementations
1005 and parameterizations. *Ocean Modelling*, 33(1), 129 - 144. Retrieved from [http://](http://www.sciencedirect.com/science/article/pii/S1463500309002418)
1006 www.sciencedirect.com/science/article/pii/S1463500309002418 doi: [https://](https://doi.org/10.1016/j.ocemod.2009.12.008)
1007 doi.org/10.1016/j.ocemod.2009.12.008
- 1008 Löhner, R., Morgan, K., Peraire, J., & Vahdati, M. (1987). Finite element flux-
1009 corrected transport (FEM-FCT) for the euler and Navier-Stokes equations. *In-*

- ternational Journal for Numerical Methods in Fluids, 7(10), 1093-1109. Retrieved
from <https://onlinelibrary.wiley.com/doi/abs/10.1002/flid.1650071007> doi:
10.1002/flid.1650071007
- Massonnet, F., Fichefet, T., Goosse, H., Vancoppenolle, M., Mathiot, P., & König Beatty,
C. (2011). On the influence of model physics on simulations of Arctic and Antarctic
sea ice. *The Cryosphere*, 5(3), 687–699. Retrieved from [https://tc.copernicus.org/
articles/5/687/2011/](https://tc.copernicus.org/articles/5/687/2011/) doi: 10.5194/tc-5-687-2011
- Massonnet, F., Goosse, H., Fichefet, T., & Counillon, F. (2014). Calibration of sea
ice dynamic parameters in an ocean-sea ice model using an ensemble Kalman fil-
ter. *Journal of Geophysical Research: Oceans*, 119(7), 4168-4184. Retrieved from
<https://agupubs.onlinelibrary.wiley.com/doi/abs/10.1002/2013JC009705> doi:
10.1002/2013JC009705
- Menemenlis, D., Fukumori, I., & Lee, T. (2005). Using Green’s Functions to Calibrate
an Ocean General Circulation Model. *Monthly Weather Review*, 133(5), 1224-1240. Re-
trieved from <https://doi.org/10.1175/MWR2912.1> doi: 10.1175/MWR2912.1
- Menemenlis, D., & Wunsch, C. (1997). Linearization of an Oceanic General Circulation
Model for Data Assimilation and Climate Studies. *Journal of Atmospheric and Oceanic
Technology*, 14(6), 1420-1443.
- Miller, P. A., Laxon, S. W., & Feltham, D. L. (2007). Consistent and contrasting decadal
Arctic sea ice thickness predictions from a highly optimized sea ice model. *Journal of
Geophysical Research: Oceans*, 112(C7). doi: 10.1029/2006JC003855
- Miller, P. A., Laxon, S. W., Feltham, D. L., & Cresswell, D. J. (2006). Optimization
of a Sea Ice Model Using Basinwide Observations of Arctic Sea Ice Thickness, Extent,
and Velocity. *Journal of Climate*, 19(7), 1089-1108. Retrieved from [https://doi.org/
10.1175/JCLI3648.1](https://doi.org/10.1175/JCLI3648.1) doi: 10.1175/JCLI3648.1
- Mu, L., Nerger, L., Tang, Q., Loza, S. N., Sidorenko, D., Wang, Q., ... Goessling, H. F.
(2020). Toward a Data Assimilation System for Seamless Sea Ice Prediction Based
on the AWI Climate Model. *Journal of Advances in Modeling Earth Systems*, 12(4),
e2019MS001937. Retrieved from [https://agupubs.onlinelibrary.wiley.com/doi/
abs/10.1029/2019MS001937](https://agupubs.onlinelibrary.wiley.com/doi/abs/10.1029/2019MS001937) (e2019MS001937 10.1029/2019MS001937) doi: 10.1029/
2019MS001937
- Nerger, L., & Hiller, W. (2013). Software for ensemble-based data assimilation
systems—implementation strategies and scalability. *Computers Geosciences*, 55,

- 110 - 118. Retrieved from <http://www.sciencedirect.com/science/article/pii/S0098300412001215> (Ensemble Kalman filter for data assimilation) doi: <https://doi.org/10.1016/j.cageo.2012.03.026>
- Nguyen, A. T., Menemenlis, D., & Kwok, R. (2011). Arctic ice-ocean simulation with optimized model parameters: Approach and assessment. *Journal of Geophysical Research: Oceans*, 116(C4). Retrieved from <https://agupubs.onlinelibrary.wiley.com/doi/abs/10.1029/2010JC006573> doi: 10.1029/2010JC006573
- Notz, D. (2012). Challenges in simulating sea ice in Earth System Models. *WIREs Climate Change*, 3(6), 509-526. Retrieved from <https://onlinelibrary.wiley.com/doi/abs/10.1002/wcc.189> doi: 10.1002/wcc.189
- Notz, D., & Stroeve, J. (2016). Observed Arctic sea-ice loss directly follows anthropogenic CO₂ emission. *Science*, 354(6313), 747-750. Retrieved from <https://science.sciencemag.org/content/354/6313/747> doi: 10.1126/science.aag2345
- Parkinson, C. L., & Washington, W. M. (1979). A large-scale numerical model of sea ice. *Journal of Geophysical Research: Oceans*, 84(C1), 311-337. Retrieved from <https://agupubs.onlinelibrary.wiley.com/doi/abs/10.1029/JC084iC01p00311> doi: 10.1029/JC084iC01p00311
- Rackow, T., Goessling, H. F., Jung, T., Sidorenko, D., Semmler, T., Barbi, D., & Handorf, D. (2016, Jun 04). Towards multi-resolution global climate modeling with ECHAM6-FESOM. Part II: climate variability. *Climate Dynamics*. doi: 10.1007/s00382-016-3192-6
- Roach, L. A., Horvat, C., Dean, S. M., & Bitz, C. M. (2018). An emergent sea ice floe size distribution in a global coupled ocean-sea ice model. *Journal of Geophysical Research: Oceans*, 123(6), 4322-4337. Retrieved from <https://agupubs.onlinelibrary.wiley.com/doi/abs/10.1029/2017JC013692> doi: 10.1029/2017JC013692
- Roach, L. A., Tett, S. F. B., Mineter, M. J., Yamazaki, K., & Rae, C. D. (2018). Automated parameter tuning applied to sea ice in a global climate model. *Climate Dynamics*, 50(1), 51-65. Retrieved from <https://doi.org/10.1007/s00382-017-3581-5> doi: 10.1007/s00382-017-3581-5
- Rostosky, P., Melsheimer, C., & Spreen, G. (2019a). *AMSR-2 winter snow depth on Arctic sea ice, Version 1.0 (NetCDF) (2012 to 2018)* [data set]. PANGAEA. Retrieved from <https://doi.org/10.1594/PANGAEA.902747> doi: 10.1594/PANGAEA.902747
- Rostosky, P., Melsheimer, C., & Spreen, G. (2019b). *AMSR-E winter snow depth on Arctic sea ice, Version 1.0 (NetCDF) (2002 to 2011)* [data set]. PANGAEA. Retrieved from

- 1076 <https://doi.org/10.1594/PANGAEA.902748> doi: 10.1594/PANGAEA.902748
- 1077 Rostosky, P., Spreen, G., Farrell, S. L., Frost, T., Heygster, G., & Melsheimer, C. (2018).
- 1078 Snow depth retrieval on arctic sea ice from passive microwave radiometers—improvements
- 1079 and extensions to multiyear ice using lower frequencies. *Journal of Geophysical Research:*
- 1080 *Oceans*, 123(10), 7120-7138. Retrieved from [https://agupubs.onlinelibrary.wiley](https://agupubs.onlinelibrary.wiley.com/doi/abs/10.1029/2018JC014028)
- 1081 [.com/doi/abs/10.1029/2018JC014028](https://agupubs.onlinelibrary.wiley.com/doi/abs/10.1029/2018JC014028) doi: 10.1029/2018JC014028
- 1082 Rothrock, D. A. (1975). The energetics of the plastic deformation of pack
- 1083 ice by ridging. *Journal of Geophysical Research (1896-1977)*, 80(33), 4514-
- 1084 4519. Retrieved from [https://agupubs.onlinelibrary.wiley.com/doi/abs/10.1029/](https://agupubs.onlinelibrary.wiley.com/doi/abs/10.1029/JC080i033p04514)
- 1085 [JC080i033p04514](https://agupubs.onlinelibrary.wiley.com/doi/abs/10.1029/JC080i033p04514) doi: 10.1029/JC080i033p04514
- 1086 Saha, S., Moorthi, S., Pan, H.-L., Wu, X., Wang, J., Nadiga, S., ... Goldberg, M. (2010).
- 1087 The NCEP Climate Forecast System Reanalysis. *Bulletin of the American Meteorological*
- 1088 *Society*, 91(8), 1015-1058. Retrieved from <https://doi.org/10.1175/2010BAMS3001.1>
- 1089 doi: 10.1175/2010BAMS3001.1
- 1090 Saha, S., Moorthi, S., Wu, X., Wang, J., Nadiga, S., Tripp, P., ... Becker, E. (2014).
- 1091 The NCEP Climate Forecast System Version 2. *Journal of Climate*, 27(6), 2185-2208.
- 1092 Retrieved from <https://doi.org/10.1175/JCLI-D-12-00823.1> doi: 10.1175/JCLI-D
- 1093 -12-00823.1
- 1094 Sein, D. V., Danilov, S., Biastoch, A., Durgadoo, J. V., Sidorenko, D., Harig, S., &
- 1095 Wang, Q. (2016). Designing variable ocean model resolution based on the observed
- 1096 ocean variability. *Journal of Advances in Modeling Earth Systems*, 8(2), 904-916. doi:
- 1097 10.1002/2016MS000650
- 1098 Semmler, T., Danilov, S., Gierz, P., Goessling, H. F., Hegewald, J., Hin-
- 1099 richs, C., ... Jung, T. (2020). Simulations for cmip6 with the awi cli-
- 1100 mate model awi-cm-1-1. *Journal of Advances in Modeling Earth Systems*, 12(9),
- 1101 e2019MS002009. Retrieved from [https://agupubs.onlinelibrary.wiley.com/doi/](https://agupubs.onlinelibrary.wiley.com/doi/abs/10.1029/2019MS002009)
- 1102 [abs/10.1029/2019MS002009](https://agupubs.onlinelibrary.wiley.com/doi/abs/10.1029/2019MS002009) (e2019MS002009 2019MS002009) doi: 10.1029/
- 1103 2019MS002009
- 1104 Semtner, A. J. (1976). A Model for the Thermodynamic Growth of Sea Ice in Numerical
- 1105 Investigations of Climate. *Journal of Physical Oceanography*, 6(3), 379-389. Retrieved
- 1106 from [https://doi.org/10.1175/1520-0485\(1976\)006<0379:AMFTTG>2.0.CO;2](https://doi.org/10.1175/1520-0485(1976)006<0379:AMFTTG>2.0.CO;2) doi:
- 1107 10.1175/1520-0485(1976)006<0379:AMFTTG>2.0.CO;2
- 1108 Sidorenko, D., Goessling, H., Koldunov, N., Scholz, P., Danilov, S., Barbi, D., ... Jung, T.

- (2019). Evaluation of fesom2.0 coupled to echam6.3: Preindustrial and highresnip simulations. *Journal of Advances in Modeling Earth Systems*, 11(11), 3794–3815. Retrieved from <https://agupubs.onlinelibrary.wiley.com/doi/abs/10.1029/2019MS001696> doi: 10.1029/2019MS001696
- Sidorenko, D., Rackow, T., Jung, T., Semmler, T., Barbi, D., Danilov, S., ... Wang, Q. (2015, Feb 01). Towards multi-resolution global climate modeling with ECHAM6-FESOM. Part I: model formulation and mean climate. *Climate Dynamics*, 44(3), 757–780. doi: 10.1007/s00382-014-2290-6
- SIMP Community. (2020). Arctic Sea Ice in CMIP6. *Geophysical Research Letters*, 47(10), e2019GL086749. Retrieved from <https://agupubs.onlinelibrary.wiley.com/doi/abs/10.1029/2019GL086749> (e2019GL086749 10.1029/2019GL086749) doi: 10.1029/2019GL086749
- Spindler, M. (1994). Notes on the biology of sea ice in the Arctic and Antarctic. *Polar Biology*, 14(5), 319–324. Retrieved from <https://doi.org/10.1007/BF00238447> doi: 10.1007/BF00238447
- Stammer, D., & Wunsch, C. (1996). The determination of the large-scale circulation of the Pacific Ocean from satellite altimetry using model Green’s functions. *Journal of Geophysical Research: Oceans*, 101(C8), 18409–18432. Retrieved from <https://agupubs.onlinelibrary.wiley.com/doi/abs/10.1029/96JC01150> doi: 10.1029/96JC01150
- Steele, M., Morley, R., & Ermold, W. (2001). PHC: A Global Ocean Hydrography with a High-Quality Arctic Ocean. *Journal of Climate*, 14(9), 2079–2087. Retrieved from [https://doi.org/10.1175/1520-0442\(2001\)014<2079:PAGOHW>2.0.CO;2](https://doi.org/10.1175/1520-0442(2001)014<2079:PAGOHW>2.0.CO;2) doi: 10.1175/1520-0442(2001)014(2079:PAGOHW)2.0.CO;2
- Stroeve, J., Hamilton, L. C., Bitz, C. M., & Blanchard-Wrigglesworth, E. (2014). Predicting September sea ice: Ensemble skill of the SEARCH Sea Ice Outlook 2008–2013. *Geophysical Research Letters*, 41(7), 2411–2418. Retrieved from <https://agupubs.onlinelibrary.wiley.com/doi/abs/10.1002/2014GL059388> doi: 10.1002/2014GL059388
- Sumata, H., Kauker, F., Gerdes, R., Köberle, C., & Karcher, M. (2013). A comparison between gradient descent and stochastic approaches for parameter optimization of a sea ice model. *Ocean Science*, 9(4), 609–630. Retrieved from <https://os.copernicus.org/articles/9/609/2013/> doi: 10.5194/os-9-609-2013
- Sumata, H., Kauker, F., Karcher, M., & Gerdes, R. (2019a, 07). Covariance of Optimal Parameters of an Arctic Sea Ice–Ocean Model. *Monthly Weather Review*, 147(7), 2579–

- 1142 2602. Retrieved from <https://doi.org/10.1175/MWR-D-18-0375.1> doi: 10.1175/MWR-
1143 -D-18-0375.1
- 1144 Sumata, H., Kauker, F., Karcher, M., & Gerdes, R. (2019b). Simultaneous Parameter
1145 Optimization of an Arctic Sea Ice–Ocean Model by a Genetic Algorithm. *Monthly Weather*
1146 *Review*, 147(6), 1899-1926. Retrieved from [https://doi.org/10.1175/MWR-D-18-0360](https://doi.org/10.1175/MWR-D-18-0360.1)
1147 .1 doi: 10.1175/MWR-D-18-0360.1
- 1148 Sumata, H., Lavergne, T., Girard-Ardhuin, F., Kimura, N., Tschudi, M. A., Kauker, F., ...
1149 Gerdes, R. (2014). An intercomparison of Arctic ice drift products to deduce uncertainty
1150 estimates. *Journal of Geophysical Research: Oceans*, 119(8), 4887-4921. Retrieved from
1151 <https://agupubs.onlinelibrary.wiley.com/doi/abs/10.1002/2013JC009724> doi:
1152 10.1002/2013JC009724
- 1153 Tschudi, M., Fowler, C., Maslanik, J., & Stroeve, J. (2010). Tracking the movement and
1154 changing surface characteristics of arctic sea ice. *IEEE Journal of Selected Topics in*
1155 *Applied Earth Observations and Remote Sensing*, 3(4), 536-540.
- 1156 Turner, A. K., Hunke, E. C., & Bitz, C. M. (2013). Two modes of sea-ice gravity drainage:
1157 A parameterization for large-scale modeling. *Journal of Geophysical Research: Oceans*,
1158 118(5), 2279-2294. Retrieved from [https://agupubs.onlinelibrary.wiley.com/doi/](https://agupubs.onlinelibrary.wiley.com/doi/abs/10.1002/jgrc.20171)
1159 [abs/10.1002/jgrc.20171](https://agupubs.onlinelibrary.wiley.com/doi/abs/10.1002/jgrc.20171) doi: 10.1002/jgrc.20171
- 1160 Turner, J., Bracegirdle, T. J., Phillips, T., Marshall, G. J., & Hosking, J. S. (2013). An
1161 Initial Assessment of Antarctic Sea Ice Extent in the CMIP5 Models. *Journal of Climate*,
1162 26(5), 1473-1484. Retrieved from <https://doi.org/10.1175/JCLI-D-12-00068.1> doi:
1163 10.1175/JCLI-D-12-00068.1
- 1164 Ungermann, M., Tremblay, L. B., Martin, T., & Losch, M. (2017). Impact of the ice
1165 strength formulation on the performance of a sea ice thickness distribution model in the
1166 arctic. *Journal of Geophysical Research: Oceans*, 122(3), 2090-2107. Retrieved from
1167 <https://agupubs.onlinelibrary.wiley.com/doi/abs/10.1002/2016JC012128> doi:
1168 10.1002/2016JC012128
- 1169 Uotila, P., Goosse, H., Haines, K., Chevallier, M., BarthÃ©lemy, A., Bricaud, C., ... Zhang,
1170 Z. (2019). An assessment of ten ocean reanalyses in the polar regions. *Climate Dynamics*,
1171 52(3), 1613–1650. Retrieved from <https://doi.org/10.1007/s00382-018-4242-z> doi:
1172 10.1007/s00382-018-4242-z
- 1173 Uotila, P., O’Farrell, S., Marsland, S., & Bi, D. (2012). A sea-ice sensitivity study
1174 with a global ocean-ice model. *Ocean Modelling*, 51, 1 - 18. Retrieved from <http://>

- 1175 www.sciencedirect.com/science/article/pii/S1463500312000625 doi: [https://](https://doi.org/10.1016/j.ocemod.2012.04.002)
1176 doi.org/10.1016/j.ocemod.2012.04.002
- 1177 Urrego-Blanco, J. R., Urban, N. M., Hunke, E. C., Turner, A. K., & Jeffery, N. (2016).
1178 Uncertainty quantification and global sensitivity analysis of the Los Alamos sea ice
1179 model. *Journal of Geophysical Research: Oceans*, 121(4), 2709-2732. doi: 10.1002/
1180 2015JC011558
- 1181 Vancoppenolle, M., Fichefet, T., Goosse, H., Bouillon, S., Madec, G., & Maqueda, M. A. M.
1182 (2009). Simulating the mass balance and salinity of Arctic and Antarctic sea ice. 1. Model
1183 description and validation. *Ocean Modelling*, 27(1), 33 - 53. Retrieved from [http://](http://www.sciencedirect.com/science/article/pii/S1463500308001613)
1184 www.sciencedirect.com/science/article/pii/S1463500308001613 doi: [https://doi](https://doi.org/10.1016/j.ocemod.2008.10.005)
1185 [.org/10.1016/j.ocemod.2008.10.005](https://doi.org/10.1016/j.ocemod.2008.10.005)
- 1186 Zampieri, L., & Goessling, H. F. (2019). Sea Ice Targeted Geoengineering Can De-
1187 lay Arctic Sea Ice Decline but not Global Warming. *Earth's Future*, 7(12), 1296-
1188 1306. Retrieved from [https://agupubs.onlinelibrary.wiley.com/doi/abs/10.1029/](https://agupubs.onlinelibrary.wiley.com/doi/abs/10.1029/2019EF001230)
1189 [2019EF001230](https://agupubs.onlinelibrary.wiley.com/doi/abs/10.1029/2019EF001230) doi: 10.1029/2019EF001230
- 1190 Zampieri, L., Goessling, H. F., & Jung, T. (2018). Bright Prospects for Arctic Sea Ice
1191 Prediction on Subseasonal Time Scales. *Geophysical Research Letters*, 45(18), 9731-
1192 9738. Retrieved from [https://agupubs.onlinelibrary.wiley.com/doi/abs/10.1029/](https://agupubs.onlinelibrary.wiley.com/doi/abs/10.1029/2018GL079394)
1193 [2018GL079394](https://agupubs.onlinelibrary.wiley.com/doi/abs/10.1029/2018GL079394) doi: 10.1029/2018GL079394
- 1194 Zampieri, L., Goessling, H. F., & Jung, T. (2019). Predictability of Antarctic Sea
1195 Ice Edge on Subseasonal Time Scales. *Geophysical Research Letters*, 46(16), 9719-
1196 9727. Retrieved from [https://agupubs.onlinelibrary.wiley.com/doi/abs/10.1029/](https://agupubs.onlinelibrary.wiley.com/doi/abs/10.1029/2019GL084096)
1197 [2019GL084096](https://agupubs.onlinelibrary.wiley.com/doi/abs/10.1029/2019GL084096) doi: 10.1029/2019GL084096
- 1198 Zampieri, L., Kauker, F., Fröhle, J., Sumata, H., Hunke, E. C., & Goessling, H. F. (2020).
1199 FESOM2 simulations with increasing sea-ice model complexity under different atmo-
1200 spheric forcings. *Zenodo*. doi: doi.org/10.5281/zenodo.4038253

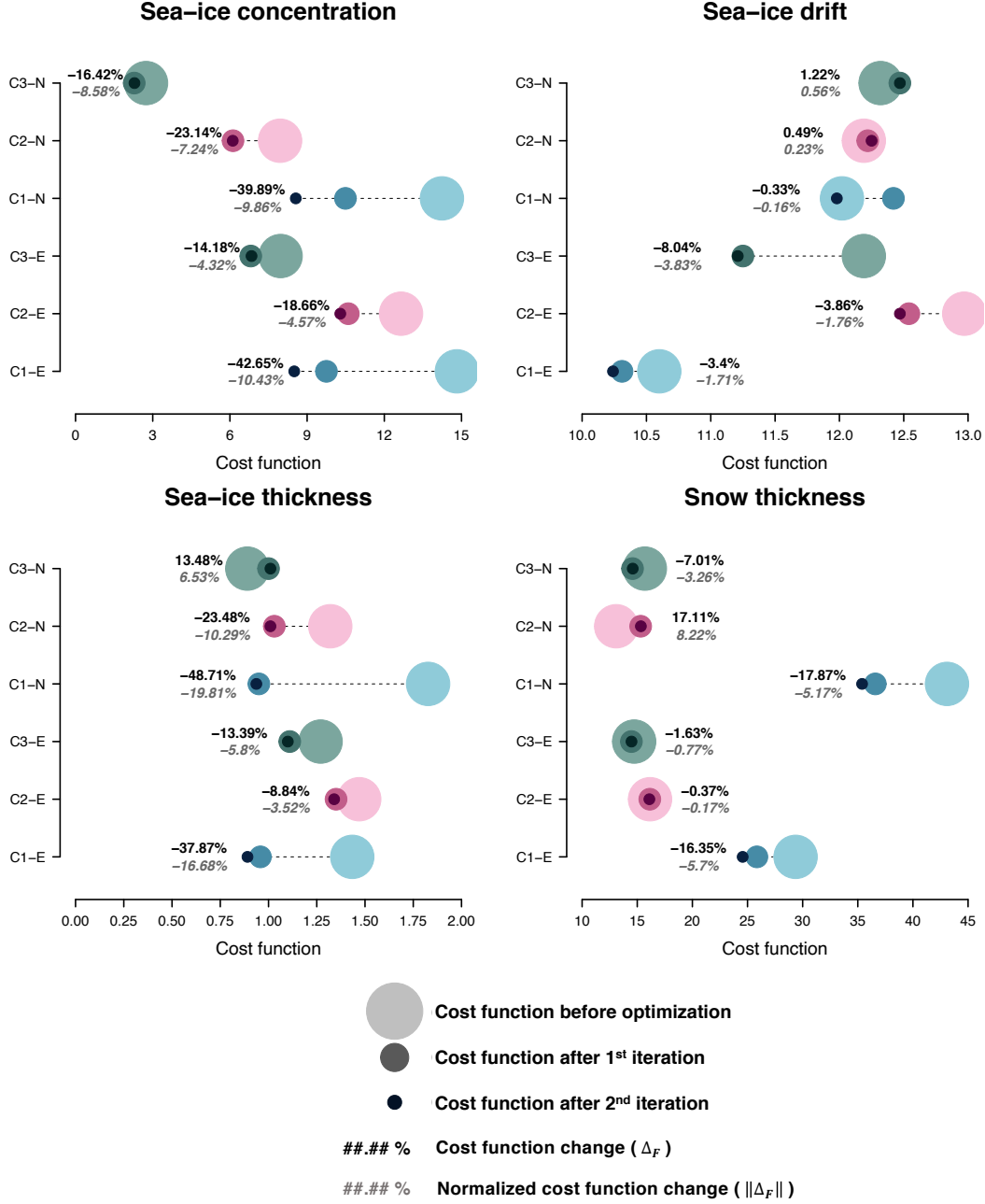


Figure 3. Cost function values for the period 2002–2015 at the three stages of the Green’s function parameter optimization (x-axis). The cost function measures the average mismatch between the state of six model configurations (y-axis) and four observational products in the Arctic region: sea-ice concentration, drift, thickness, and snow thickness (only the first three observation types are used in the Green’s function optimization). The suffixes “-E” and “-N” indicate the employment of the ERA5 and NCEP atmospheric reanalysis used to force the three model setups C1, C2, and C3, respectively. The percentages in black font indicate the cost function change Δ_F induced by the optimization. The percentages in gray font refer to $\|\Delta_F\|$, the normalized formulation of the cost function change.

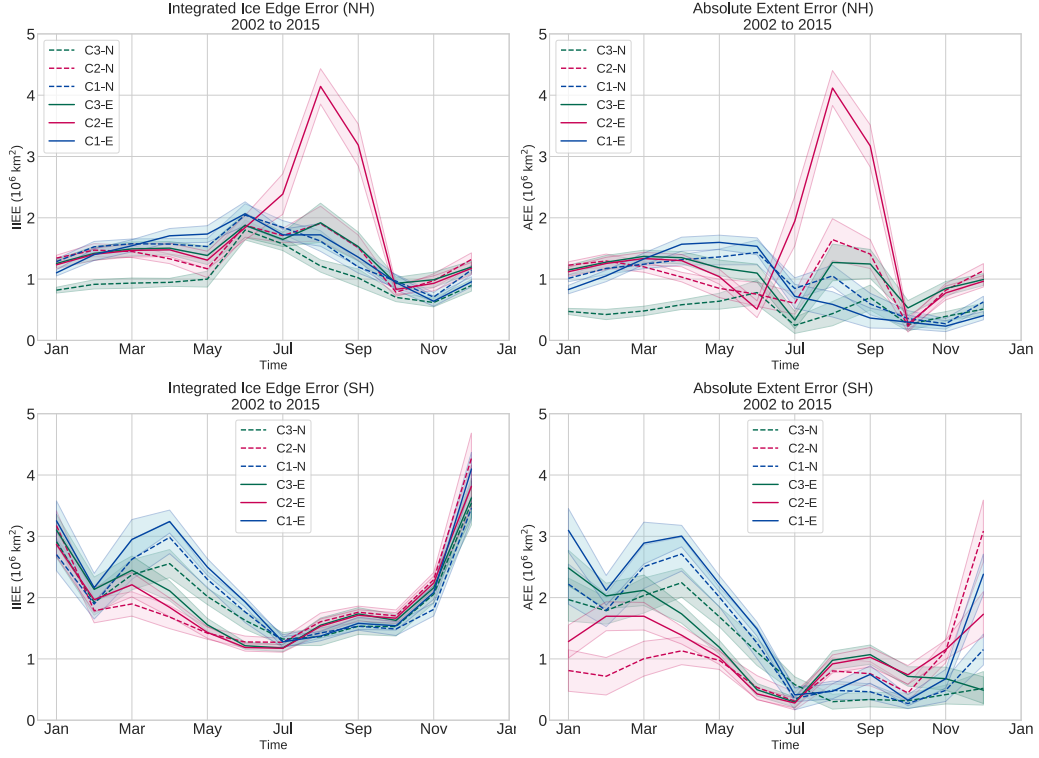


Figure 4. Seasonal variation of the northern hemisphere (top) and southern hemisphere (bottom) Integrated Ice Edge Error (IIEE) and Absolute Extent Error (AEE) for six optimized model configurations (C1-E to C3-N) averaged over the period 2002–2015. The IIEE and AEE are computed based on the monthly median ice edge, which is defined as the 15% contour line of the sea-ice concentration. The shading indicates the $\sim 95\%$ confidence intervals, based on standard errors obtained from the fourteen individual monthly values.

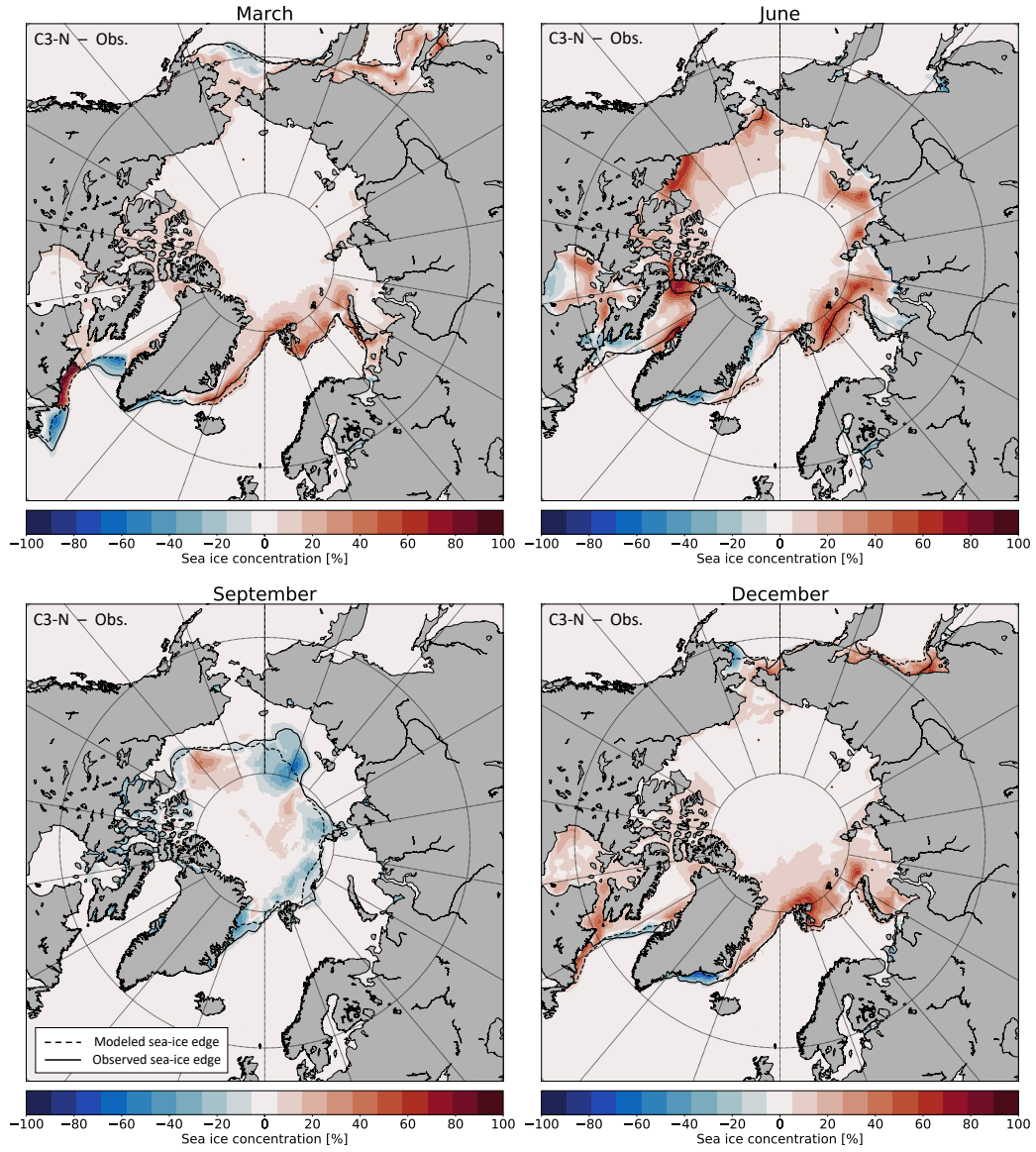


Figure 5. 2002–2015 average sea-ice concentration anomaly (C3-N - Obs.) for the months of March, June, September, and December. The modelled and observed sea-ice edges, corresponding to the 15% sea-ice concentration contour, are represented respectively by the dashed and solid black lines.

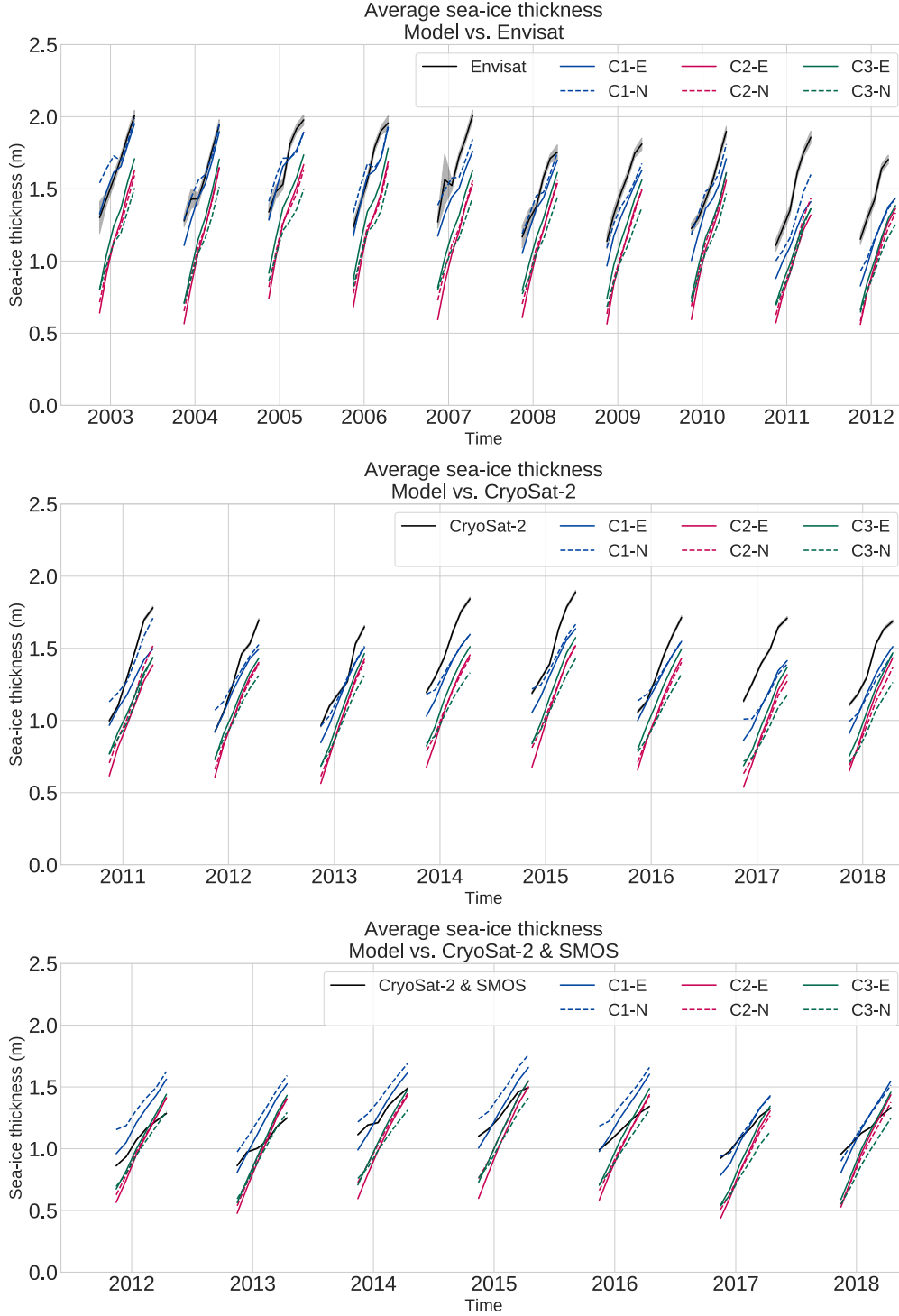


Figure 6. November to April average sea-ice thickness for six model configurations (C1-E to C3-N) and for the Envisat (top plot), CryoSat-2 (middle plot), and CryoSat-2/SMOS (bottom plot) satellite observations. The ~95% confidence intervals of the observations are indicated by the gray shading (not visible for CryoSat-2 and CryoSat-2/SMOS), based on 2 standard deviations of the average sea-ice thickness computed through error propagation assuming spatially uncorrelated uncertainties (which is not necessarily the case). The monthly averaged model results have been restricted to the locations within the satellites' orbits ($< 81.45^\circ\text{N}$ for Envisat and $< 87^\circ\text{N}$ for CryoSat-2) by the application of a large-scale spatial mask where monthly observations and model data are available simultaneously.

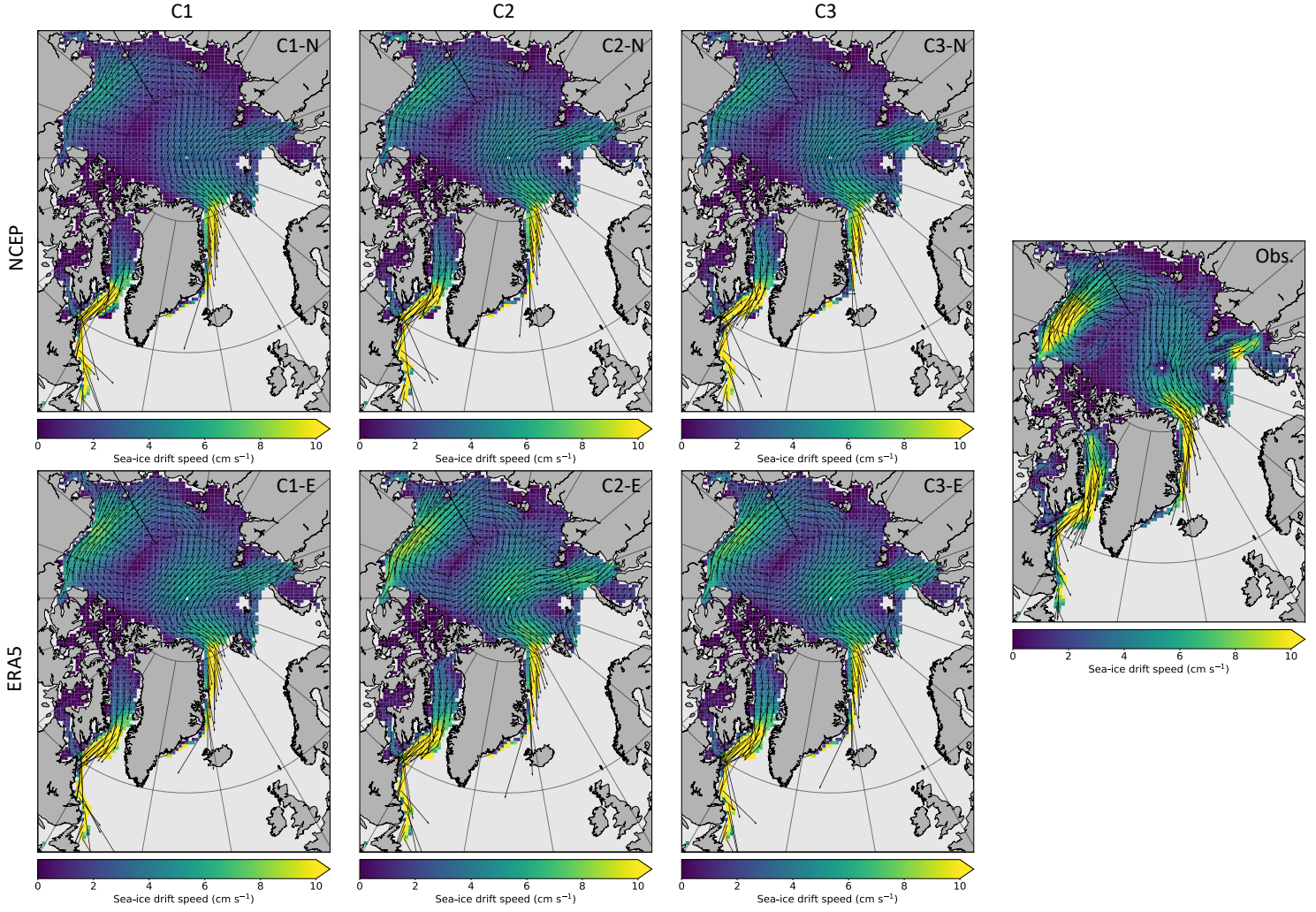


Figure 7. April 2015 monthly averaged sea-ice drift speed of six model configurations (C1-N to C3-E) and of the OSI-405 observations.

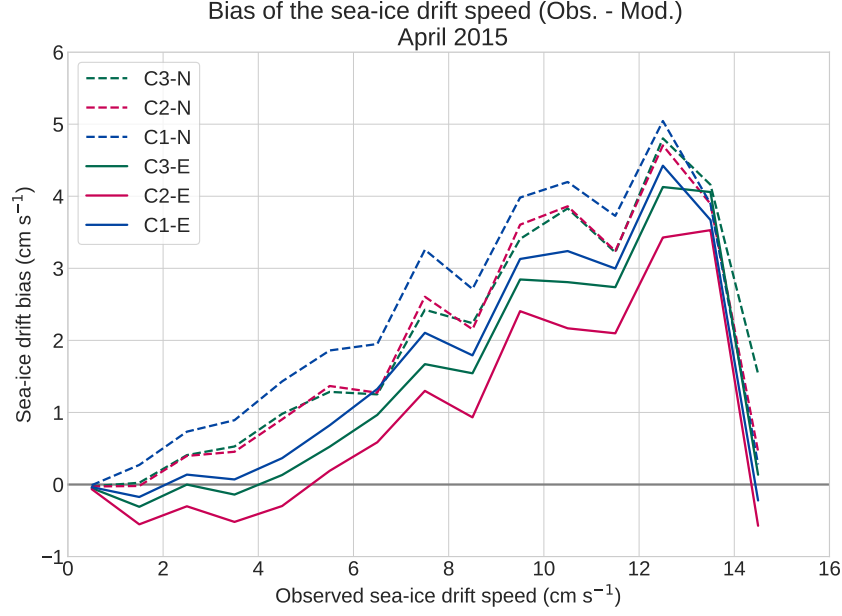


Figure 8. April 2015 sea-ice drift speed bias (observation – model; y-axis) for six model configurations (C1-N to C3-E) as function of the of the observed OSI-405 sea-ice drift speed (x-axis). The plot is constructed by dividing the observed sea-ice drift speed in equally spaced intervals of width 1 cm s^{-1} , for which the corresponding bias values are grouped and averaged. We do not consider observed sea-ice speeds $\mathbf{v}_{ice} > 15 \text{ cm s}^{-1}$ because of the low number of observational points and of the consequent low significance of the results.

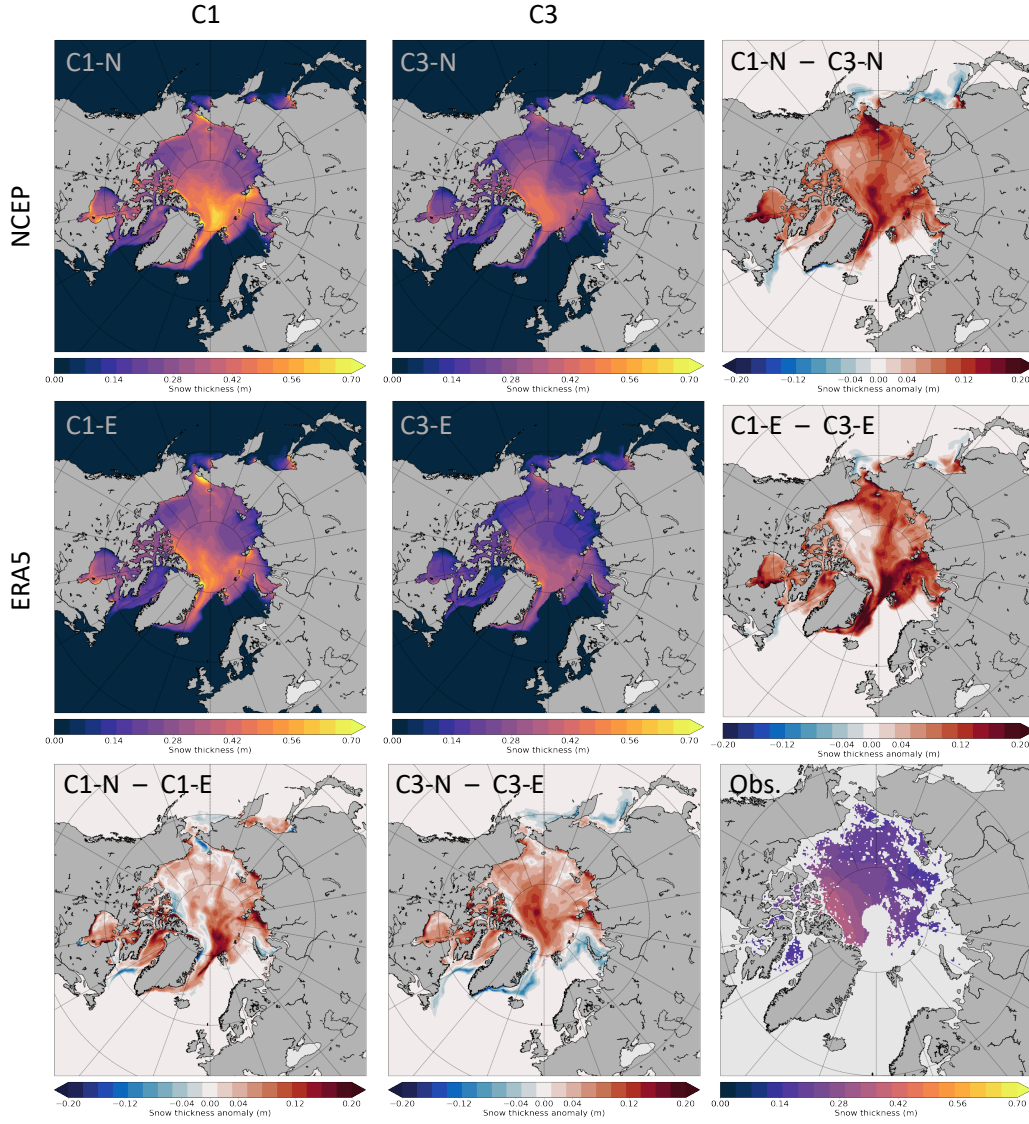


Figure 9. April snow thickness and snow thickness anomalies averaged over the period 2002–2015 for four configurations: C1-N, C1-E, C3-N, and C3-E. The C2 setup has not been displayed because its results in terms of snow thickness are very similar to the C3 setup. The April snow thickness observations averaged over the same period are mapped in the bottom-right corner of the panel.

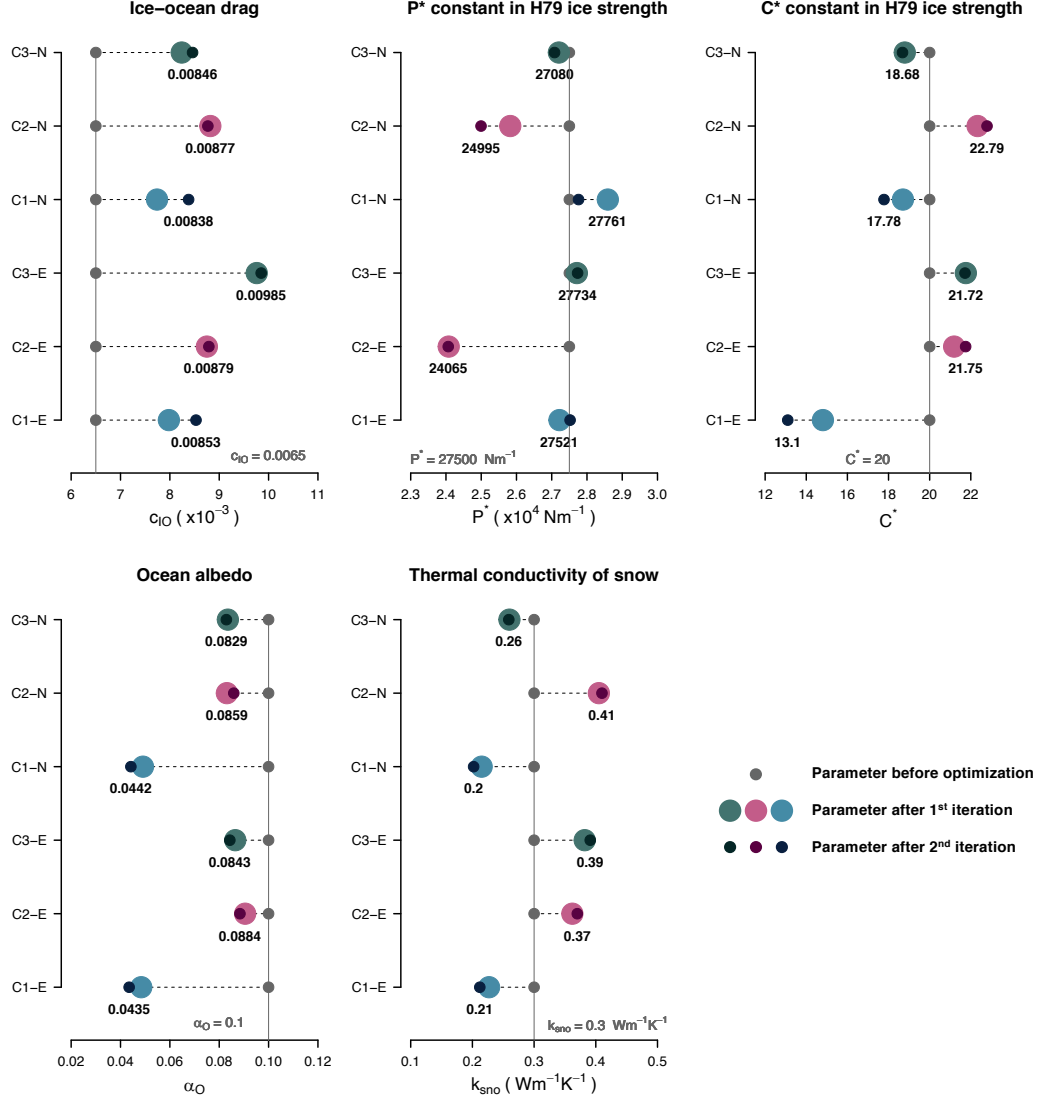


Figure 10. Model parameters (x-axis) at three stages of the Green's function parameter optimization. The control values of the parameters are indicated in gray. For each setup, the numerical value of the optimized parameters is reported in black below each point. Only the parameters common to the C1, C2, and C3 model setups are shown. The suffixes “-E” and “-N” indicate respectively the ERA5 and NCEP atmospheric reanalysis used to force the three model setups.

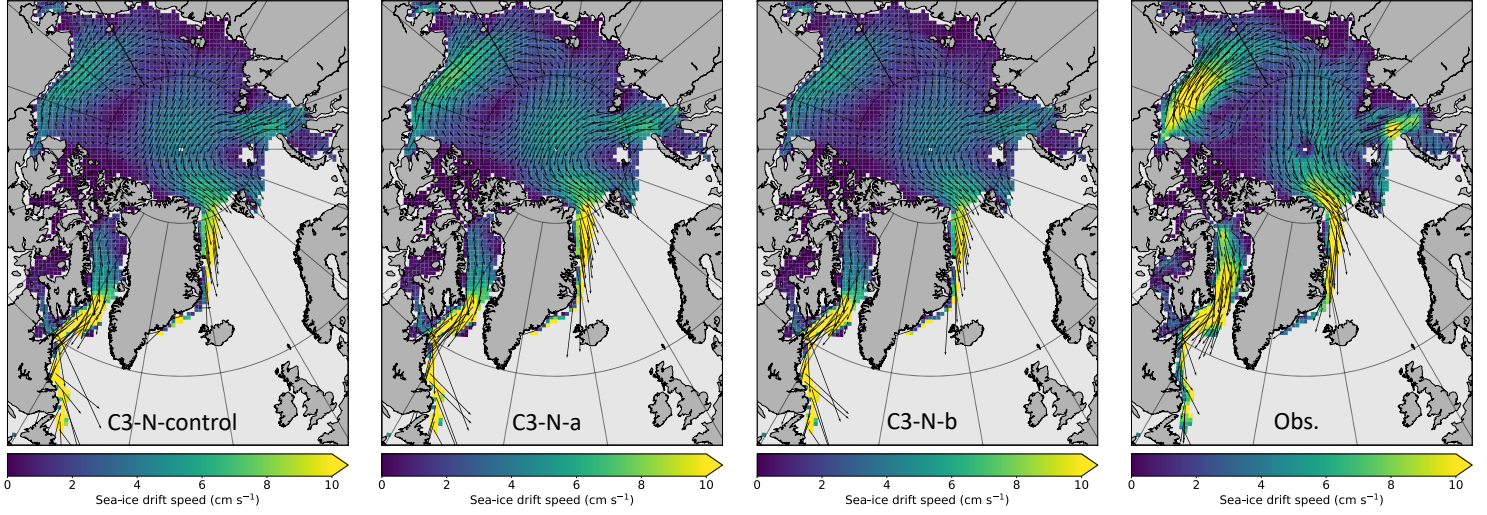


Figure 11. April 2015 monthly averaged sea-ice drift speed of C3-N-control, C3-N-a, C3-N-b, and of the OSI-405 observations.

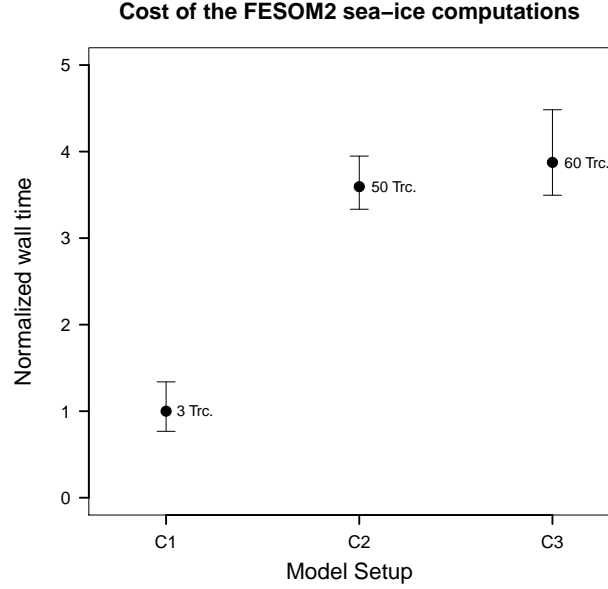


Figure 12. Relative computational cost of the sea-ice component of three FESOM2 setups (C1, C2, and C3). The values are normalized by the C1 wall time. All the simulations run on the same machine, with the same computational mesh, and under the ERA5 forcing. The bars indicate the maximum and minimum values registered among the computing CPUs. The number of tracers advected in each setup is also reported.